

Droplet Actuation on Various Electrode Shapes in Electrowetting-based Microfluidics

Negar Rajabi

A Thesis

in

The Department

of

Mechanical and Industrial Engineering

Presented in Partial Fulfillment of the Requirements

for the Degree of Master of Applied Science (Mechanical Engineering) at

Concordia University

Montreal, Quebec, Canada

November 2009

© Negar Rajabi, 2009



Library and Archives
Canada

Published Heritage
Branch

395 Wellington Street
Ottawa ON K1A 0N4
Canada

Bibliothèque et
Archives Canada

Direction du
Patrimoine de l'édition

395, rue Wellington
Ottawa ON K1A 0N4
Canada

Your file *Votre référence*
ISBN: 978-0-494-67154-2
Our file *Notre référence*
ISBN: 978-0-494-67154-2

NOTICE:

The author has granted a non-exclusive license allowing Library and Archives Canada to reproduce, publish, archive, preserve, conserve, communicate to the public by telecommunication or on the Internet, loan, distribute and sell theses worldwide, for commercial or non-commercial purposes, in microform, paper, electronic and/or any other formats.

The author retains copyright ownership and moral rights in this thesis. Neither the thesis nor substantial extracts from it may be printed or otherwise reproduced without the author's permission.

AVIS:

L'auteur a accordé une licence non exclusive permettant à la Bibliothèque et Archives Canada de reproduire, publier, archiver, sauvegarder, conserver, transmettre au public par télécommunication ou par l'Internet, prêter, distribuer et vendre des thèses partout dans le monde, à des fins commerciales ou autres, sur support microforme, papier, électronique et/ou autres formats.

L'auteur conserve la propriété du droit d'auteur et des droits moraux qui protègent cette thèse. Ni la thèse ni des extraits substantiels de celle-ci ne doivent être imprimés ou autrement reproduits sans son autorisation.

In compliance with the Canadian Privacy Act some supporting forms may have been removed from this thesis.

While these forms may be included in the document page count, their removal does not represent any loss of content from the thesis.

Conformément à la loi canadienne sur la protection de la vie privée, quelques formulaires secondaires ont été enlevés de cette thèse.

Bien que ces formulaires aient inclus dans la pagination, il n'y aura aucun contenu manquant.


Canada

Abstract

Droplet Actuation on Various Electrode Shapes in Electrowetting-based Microfluidics

Negar Rajabi

Electrowetting has been widely used in digital microfluidics as a reliable actuation method due to its considerable advantages such as the absence of heat generation, rapid switching response, flexibility, and low power consumption. Research on the improvement of this method has turned into one of the attractive fields in the design of fluid handling micro devices. This work presents a combined numerical and experimental study to investigate the effect of electrode shape in electrowetting-based microsystems. A new crescent-shaped electrode is proposed which provides a uniform actuation force at the contact line as well as overlap between the adjacent electrodes. The onset of actuation and droplet mobility on electrode arrays have been investigated. The numerical method is based on the Volume of Fluid technique to track the 3-D interface along with the Laplace equation solver to calculate the electric field in the domain. Furthermore, the dynamic behaviour of tri-phase contact line is modeled using the molecular-kinetic theory. Validation experiments were carried out to characterize the droplet actuation on various electrode shapes. The superior performance of the new electrode shape is demonstrated by comparing the droplet velocity and deformation, as well as contact angle distribution with those of a simple flat electrode. Using crescent electrode, the droplet actuation occurs with less deformation and higher velocities. The velocities obtained by using the crescent electrode are up to 4 times at the onset of the actuation and 2 times at the steady state motion of those on the flat electrode. The novel crescent shape can even actuate the droplets which are not placed on the electrode.

Acknowledgement

I would like to express my sincere appreciation to Dr. Ali Dolatabadi for his guidance, support and patience throughout this research. This thesis would not have been possible without his tremendous encouragement. Special thanks and gratitude is owed to my colleagues Khalid Koraitem and Toka Zaini who helped me in carrying out the experiments. I would also like to thank Niyusha Samadi for the design of the microfluidics test rig. I appreciate the help of McGill Nanotools Microfab laboratory staff for providing useful advices during the fabrication procedure.

I would like to acknowledge Simulent Inc., Toronto, Ontario for providing access to the SIMULENT code which is modified for the present simulations. I am also grateful for the support from MDEIE-SIRII and Le Fonds québécois de la recherche sur la nature et les technologies (FQRNT).

CONTENTS

LIST OF FIGURES.....	VII
NOMENCLATURE.....	XI
1. BACKGROUND AND MOTIVATION.....	1
1.1. CONTINUOUS AND DIGITAL MICROFLUIDICS	2
1.2. ACTUATION PRINCIPLES.....	4
1.3. ELECTROWETTING CONCEPT AND APPLICATIONS	7
1.4. ELECTRODE SHAPE	15
1.5. OBJECTIVES.....	19
1.6. THESIS STRUCTURE	19
2. NUMERICAL TECHNIQUE	20
2.1. DROPLET DYNAMICS	20
2.1.1. <i>Governing Equations</i>	21
2.1.2. <i>Boundary and Initial Conditions</i>	25
2.1.3. <i>Timestep Restrictions</i>	28
2.2. ELECTRIC POTENTIAL	29
2.3. DYNAMIC CONTACT ANGLE.....	35
3. EXPERIMENTAL APPROACH	39
3.1. MICROFABRICATION	39
3.1.1. <i>Photomask</i>	40
3.1.2. <i>Electrode Layer</i>	41

3.1.3. <i>Insulating Layer</i>	46
3.1.4. <i>Hydrophobic Layer</i>	51
3.2. EXPERIMENTAL SETUP	53
3.3. GEOMETRY	54
4. RESULTS AND DISCUSSIONS.....	56
4.1. MODEL IMPROVEMENT.....	56
4.2. DROPLET MORPHOLOGY	66
4.3. DROPLET VELOCITY	69
4.3.1. <i>Single Electrode</i>	70
4.3.2. <i>Electrode Array</i>	74
5. CLOSURE	76
5.1. SUMMARY AND CONCLUSIONS	76
5.2. ONGOING AND FUTURE WORK	77
BIBLIOGRAPHY	80
APPENDIX A: PARYLENE DEPOSITION FORMULAS.....	89

LIST OF FIGURES

Figure 1-1 A continuous flow microfluidic device [1].....	3
Figure 1-2 Droplet creation, motion, splitting, and merging in a digital microfluidic device [2].....	4
Figure 1-3 the equilibrium forces on a droplet at rest on a solid substrate.....	5
Figure 1-4 A schematic of a capillary with a radius of r placed in a pool of liquid	5
Figure 1-5 Surface tension gradient for a droplet (a) sitting on a surface (b) in a microchannel	7
Figure 1-6 Schematic of a droplet (a) not actuated (b) in the presence of the electric potential.....	8
Figure 1-7 EDL, stern and diffuse layers.....	9
Figure 1-8 Droplet actuation via electrowetting (the darker electrode is fired)	11
Figure 1-9 Different electrode shapes (a) flat (b) interdigitated (c) crescent	17
Figure 1-10 Interdigitated electrodes (a) sinusoidal (b) rectangular (c) triangular.....	18
Figure 2-1 Volume fraction advection in 2D (a) an exact liquid interface, (b) corresponding $f_{i,j}$ and the associated planar interfaces, (c) with u positive, the region to the right of the dashed line is advected into the neighboring cell [37].	23
Figure 2-2 Free surface boundary conditions in 2D (a) tangential velocity (b) new fluid velocity; for both cases $u_{i+\frac{1}{2},j} = u_{i+\frac{1}{2},j-1}$ [37].....	27

Figure 2-3 Contact angle change (a) before applying the voltage (b) after applying the voltage [33]	31
Figure 2-4 Effective interfacial voltage on substrate cells using the cell averaging method.....	33
Figure 2-5 Schematic of voltage distribution using the new voltage implementation (a) before defining droplet location (b) after placing the droplet (c) a larger view of section A	34
Figure 2-6 The numerical algorithm applied in this study.....	38
Figure 3-1 Schematic of microchannel plates with different layers of coatings.....	40
Figure 3-2 Top view of designed mask (a) printed mask (b) magnified image of section A	41
Figure 3-3 Electrode deposition machines (a) Denton RF (b) MRC 603	42
Figure 3-4 Photolithography equipments (a) BidTec spin-coater (b) EVG620.....	45
Figure 3-5 Voltage breakdown of Parylene C layer versus its thickness [from SCS company].....	47
Figure 3-6 Parylene structure and composition [67].....	48
Figure 3-7 Parylene coating machine, PARA-10S	50
Figure 3-8 Thickness measurement of Parylene layer using AFM.....	51
Figure 3-9 Thickness measurement of Teflon layer using surface profiler	52
Figure 3-10 Experimental setup.....	53
Figure 3-11 Geometry of flat and crescent electrodes	55
Figure 4-1 Static contact angle of a droplet sitting on a Teflon surface.....	57

Figure 4-2 Schematic view of droplet contact angle on the Teflon surface actuated at 55 V (a) Static (b) Dynamic	58
Figure 4-3 Droplet velocity on an array of flat electrodes for static and dynamic models	59
Figure 4-4 Interfacial voltage distribution (a) using average voltage (b) using new voltage implementation.....	60
Figure 4-5 A 3D schematic of electric field applied on the droplet in a channel	61
Figure 4-6 Droplet velocity on an array of flat electrodes with and without voltage correction.....	62
Figure 4-7 Actuated droplet contact line on flat electrode (a) at the electrode end (b) at the beginning of the electrode.....	63
Figure 4-8 Droplet velocity based on trailing edge, mid-point, and leading edge.....	64
Figure 4-9 Droplet velocity on an array of flat electrodes using previous and modified models	66
Figure 4-10 Experimental and numerical results for droplet advancement on a single electrode (a) flat (b) crescent.....	67
Figure 4-11 Contact angle distribution of a droplet on a single electrode (a) flat (b) crescent.....	68
Figure 4-12 Experimental and numerical results of droplet velocity on a single electrode for various droplet diameters (a) $D=1500 \mu\text{m}$ (b) $D=1600 \mu\text{m}$ (c) $D=1700 \mu\text{m}$ (d) $D=1800 \mu\text{m}$ (e) $D=1900 \mu\text{m}$ (f) $D=2000 \mu\text{m}$	71
Figure 4-13 Droplet maximum velocity on a single electrode for various droplet sizes..	72
Figure 4-14 Actuation at 55 V for a droplet with the diameter of $2000 \mu\text{m}$ touching the electrode in a channel with the height of $200 \mu\text{m}$ (a) flat (b) crescent.....	73

Figure 4-15 Actuation at 55 V for a droplet with the diameter of 1900 μm in a channel with the height of 300 μm (a) touching flat electrode (b) 20 μm far from crescent electrode	73
Figure 4-16 Numerical results of droplet movement on array of electrodes (a) flat (b) crescent.....	74
Figure 4-17 Comparison between droplet velocity and oscillation on flat and crescent arrays	75
Figure 5-1 Two-way crescent array	78

NOMENCLATURE

C	capacitance
d	insulator thickness
D	droplet diameter
\vec{D}	electric flux density
\vec{E}	electric field
\vec{F}_b	body forces
\vec{F}_{ST}	surface tension volumetric force
f	volume fraction
g	gravitational acceleration
k	curvature
k^0	characteristic frequency
k_B	Boltzmann constant
L	electrode length
\hat{n}	unit normal vector
p	pressure
R	radius of curvature
S	interface area
t	time
\hat{t}	unit tangential vector
T	absolute temperature
Δt	timestep
u	velocity in x direction

v	velocity in y direction
V	velocity
w	velocity in z direction
W	electrode width
Δx	grid size in x direction
Δy	grid size in y direction
Δz	grid size in z direction

Greek letters

α	polar angle
γ_{LG}	surface tension at liquid-gas interface
γ_{SG}	surface tension at solid-gas interface
γ_{SL0}	initial surface tension at solid-liquid interface
γ_{SL}	surface tension at solid-liquid interface
ϵ_0	permittivity of the air
ϵ_l	permittivity of the insulator
θ_0	non-actuated contact angle
θ_D	dynamic contact angle
θ_s	static contact angle
θ_v	contact angle after actuation
λ	average molecular displacement
μ	viscosity
ξ	friction coefficient

ρ	fluid density
$\tilde{\tau}$	shear stress tensor
ψ	electric potential
$\tilde{\psi}$	Electric potential at the interface

Subscripts and superscripts

i,j,k	grid number
l,m,n	grid number
g,l,s	gas, liquid, solid
n	timestep
new	new value
old	old value

1. BACKGROUND AND MOTIVATION

Over the past decades, considerable effort has been invested to develop fabrication techniques for realization of miniaturized instruments and systems such as lab-on-a-chip (LOC) devices. The goal of such devices is to replace the room-sized laboratory. Reductions in the amount of required samples and reagents, shorter analysis time, high throughput, automation and portability are some of the main advantages of such devices. With this goal in mind, a great number of microfluidic components such as pumps, valves, channels, sensors, mixers and dispensers have been designed and fabricated in recent years. A lab-on-a-chip device which is utilised in biomedical analysis mainly uses liquids as its media. These liquids mostly contain blood, protein, DNA, antibody, and buffer solutions.

Surface tension is the dominant force in micro-scale fluidic devices. The concept of varying interfacial tension to move liquids have been used in several techniques such as thermocapillary surfactants, dielectrophoresis, and electrowetting actuations. Among these methods, electrowetting has distinct advantages such as the absence of heat generation, rapid switching response, the absence of mechanical parts, and low power consumption. Therefore, electrowetting is considered to be a reliable means of actuation in digital microfluidics.

1.1. CONTINUOUS AND DIGITAL MICROFLUIDICS

Most of the microfluidic technologies are based on a continuous flow inside microchannels (Figure 1-1). The movement of liquid along these micron-sized paths has been made possible by different methods of manipulating the flow such as external pressure sources, external mechanical pumps, integrated mechanical micropumps, or electrokinetic mechanisms. In a typical microfluidic system, various bulk fluids continuously mix, react, or separate inside microchannels. These types of systems are useful for many simple and well-defined applications; however they are not still suitable to be used in complex applications due to the lack of sufficient flexibility, scalability, and reconfigurability which are needed in such systems of detailed structures. The difficulty in dealing with the continuous flows comes from the fact that the governing parameters of the flow field, for example pressure, fluid resistance, and electric field, vary along the flow path. As a result, at each location in the system the flow is dependent on the properties of the entire system. In the case of flow mixing and reaction, the flow behaviour becomes more unpredictable due to the changes in electrical and

hydrodynamic properties. Accordingly, the design and analysis of such a system is challenging. These systems are suitable only for a narrow class of applications with pre-determined tasks and functions.



Figure 1-1 A continuous flow microfluidic device [1]

Alternatively, using discrete independently controllable droplets provides several advantages over the bulk flow systems (Figure 1-2). This method allows having a repeating small set of operations which can be combined to generate larger sets. The digitization method facilitates the use of a hierarchical and cell-based approach for microfluidics. Thus, digital microfluidics offers a novel flexible and scalable fluid manipulation system. Moreover, the unit cells in a microfluidic array can be reconfigured to change their functionality in the device. In addition, the amount of required samples and reagents decreases using the digital systems. Understanding the discrete flow behaviour in a basic cell component allows the design and analysis of complex microfluidic chips. Electrowetting-on-dielectric (EWOD) is a common actuation method

which has recently been utilised in many LOC devices. EWOD uses the concept of droplet dynamics under the electric field which is described in the following section.

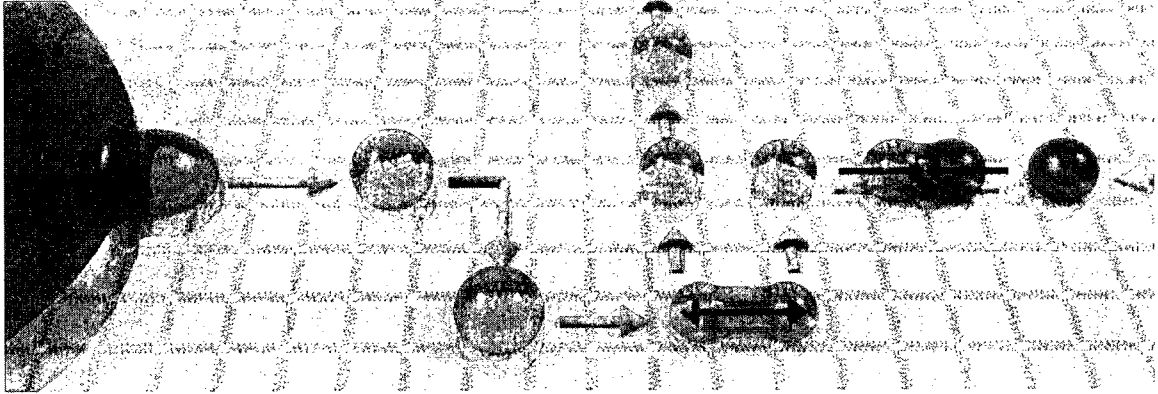


Figure 1-2 Droplet creation, motion, splitting, and merging in a digital microfluidic device [2]

1.2. ACTUATION PRINCIPLES

Figure 1-3 shows the forces applied on a stationary liquid droplet sitting on a hydrophobic solid surface. γ_{SG} , γ_{SL} , and γ_{LG} are the solid-gas, solid-liquid, and liquid-gas surface tensions, respectively. The gravity force is neglected because of small sizes of droplet. Contact angle θ is applied on the contact line as the equilibrium contact angle and defines the angle between the solid-liquid and liquid-gas surface tensions Young's equation (Equation (1-1)) describes the relationship between the surface tension forces at the solid-liquid-gas interface. This dependence of the contact angle with the surface tension forces exists before contact angle saturation which is when the value of the solid/liquid interfacial tension reaches zero.

$$\gamma_{SG} - \gamma_{SL} = \gamma_{LG} \cos\theta \quad (1-1)$$

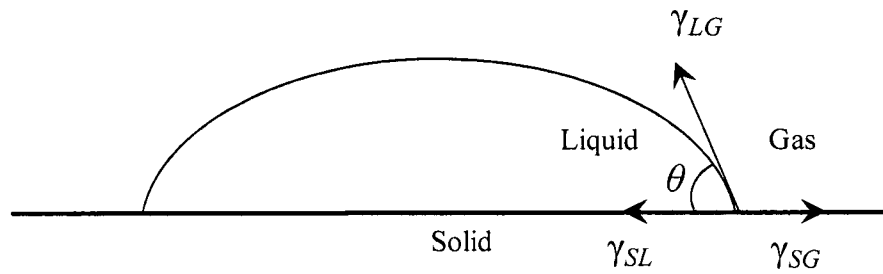


Figure 1-3 the equilibrium forces on a droplet at rest on a solid substrate

According to the Young's equation, in a small capillary with the radius of r which is open at both ends as shown in Figure 1-4, the liquid rises when it is placed in a pool of liquid. In this case, the total energy reduction, $(\gamma_{SG} - \gamma_{SL})2\pi rh$, should be balanced by the work done to raise the column of liquid, $\Delta p\pi r^2 h$. Equating these two terms presents Young-Laplace equation.

$$\Delta p = \frac{2(\gamma_{SG} - \gamma_{SL})}{r} = \frac{2\gamma_{LG} \cos \theta}{r} \quad (1-2)$$

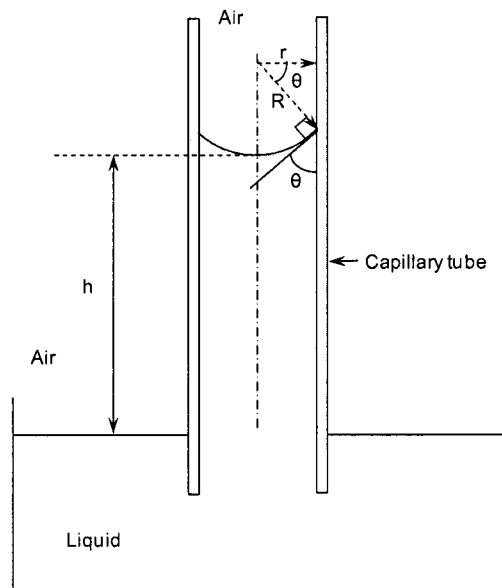


Figure 1-4 A schematic of a capillary with a radius of r placed in a pool of liquid

The general form of Equation (1-2) for an arbitrarily curved surface is,

$$\Delta p = \gamma \left(\frac{1}{R_1} + \frac{1}{R_2} \right) \quad (1-3)$$

where γ is the surface tension, R_1 and R_2 are the principal radii of curvature of the surface. For a droplet in contact with a surface having a gradient of surface tension, non-equal surface tension forces applied on the contact line create a net force between the two sides of droplet. This force may cause the droplet movement as shown in Figure 1-5 (a). Chaudhury and Whitesides [3] have shown one of the most straightforward manifestations of this phenomenon. They showed that a surface with a spatial gradient in its surface tension can make sitting drops of water move uphill because of an imbalance in the forces acting on the contact line of the drop. They provided a surface with variable surface tension by exposing it to the diffusing front of a vapour of decyltrichlorosilane. Thus, they moved the droplets from the more hydrophobic end of the surface, inclined 15° , up toward the hydrophilic end with a velocity of 1-2 mm/s. Similarly, for a droplet confined in a microchannel (Figure 1-5 (b)), the gradient of liquid-gas interfacial tension may generate a force to move the droplet.

Contact lines are characterized by a range of contact angles rather than a single equilibrium one [4,5]. Contact angle measured for a liquid advancing across a surface without the interfacial area decreasing is called the advanced contact angle. Contact angle measured for a liquid receding from the surface before the interfacial area increases is called receded contact angle. An advanced contact line has a higher contact angle, θ_A , than a receded one, θ_R . Contact angle hysteresis is defined as the difference between θ_A

and θ_R . For a droplet at equilibrium, the contact angle changes between these two values; thus an additional force is needed to start the droplet motion.

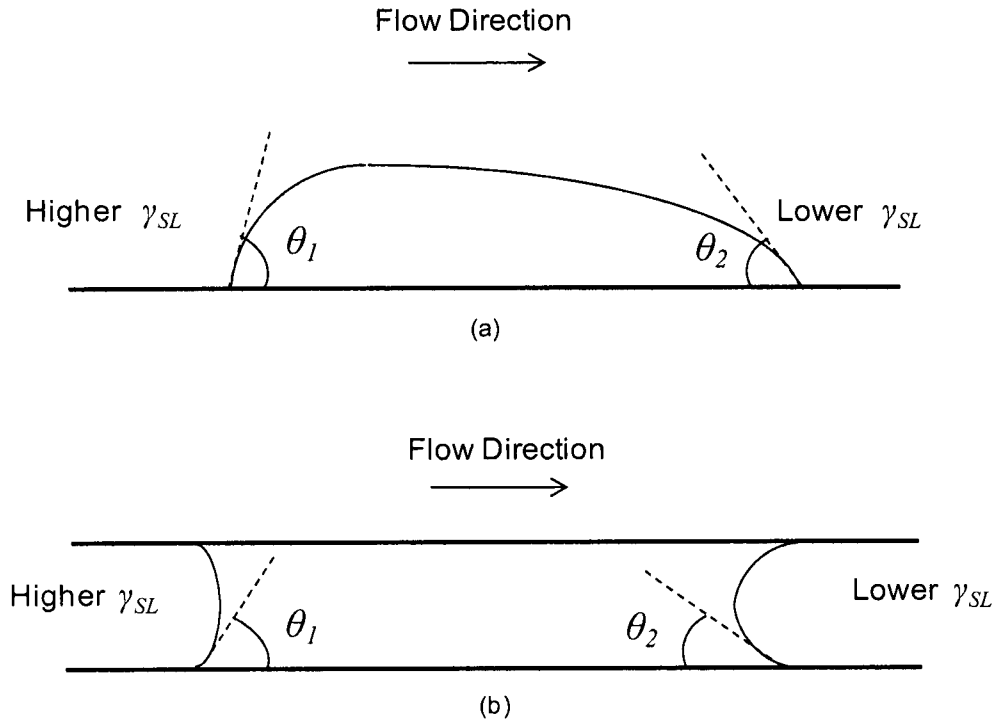


Figure 1-5 Surface tension gradient for a droplet (a) sitting on a surface (b) in a microchannel

1.3. ELECTROWETTING CONCEPT AND APPLICATIONS

Electrowetting is a reliable means of actuation in digital microfluidics. The concept of electrowetting is to change the free surface tension of liquid by applying an external electric field. As it is shown in Figure 1-6 (a), droplet has an equilibrium contact angle above 90° when placed on a hydrophobic surface. Figure 1-6 (b) shows the same droplet after applying the electric field. By applying the voltage, the surface tension at solid-liquid interface, γ_{SL} , is altered. The contact angle changes according to Young's equation

(Equation (1-1)) and consequently the surface changes from hydrophobic to hydrophilic where the final contact angle is below 90° .

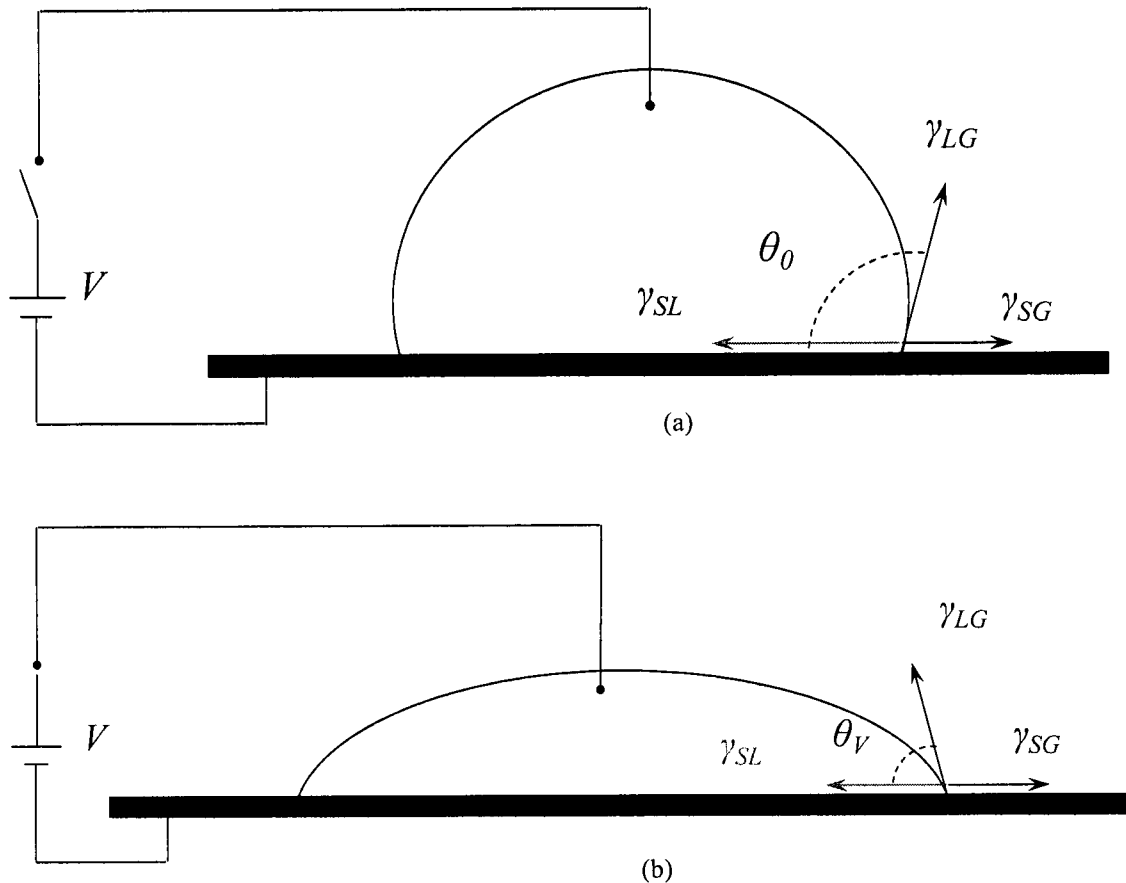


Figure 1-6 Schematic of a droplet (a) not actuated (b) in the presence of the electric potential

When an electric field is applied, the charges at the solid substrate attract the ions in the liquid as shown in Figure 1-7. Therefore, the charge concentration increases at the contact line of the droplet. The layer of ions strongly attracted to the solid surface is called the stern layer. There is a layer with the gradual decrease in charge density from stern layer to the electrically neutral bulk fluid. This layer is called the diffuse layer. Stern and diffuse layer together are called the electric double layer, EDL.

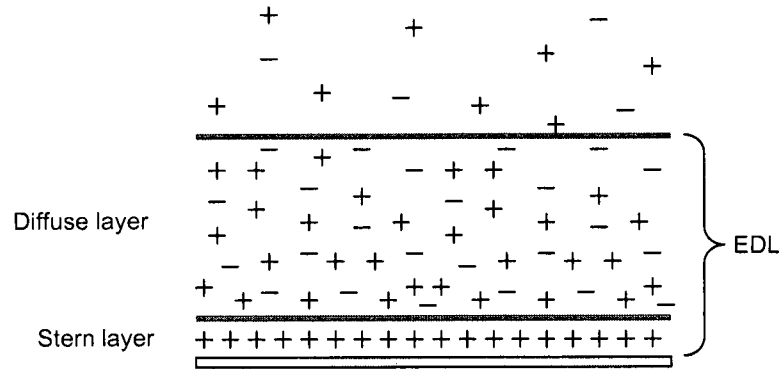


Figure 1-7 EDL, stern and diffuse layers.

Because of small thickness of the EDL (about 1 nm), there is not considerable amount of energy stored in this layer. Therefore, a dielectric layer (800 nm of parylene C in this study) is used on the electrodes. This is called Electrowetting on Dielectric, EWOD. Since the energy stored in the dielectric is much more than the energy which is stored in the EDL, the effect of electric double layer is neglected in modeling the phenomenon.

The capacitance model is a common approach to study the electrowetting phenomenon [6]. In this model, the energy stored in a capacitor is added to the Young's equation (Equation (1-1)). The presence of an external electric field affects the free charges in the liquid which leads to their rearrangement. The resultant Coulombic force in the interface is the driving force for the liquid. In this thesis, capacitor approach is used to model the electrowetting on dielectric phenomenon. In EWOD, there is no current going through the droplet-solid interface. The energy stored in the dielectric layer may be calculated as,

$$E = \frac{1}{2} C \psi^2 = \frac{\epsilon_0 \epsilon_l}{2d} \psi^2 \quad (1-4)$$

Where $\varepsilon_0 \varepsilon_l$ is the dielectric constant of the insulator layer, d is the dielectric thickness, and ψ is the applied voltage. This electrostatic energy modifies the solid-liquid interfacial tension as shown below.

$$\gamma_{SL}(V) = \gamma_{SL}(0) - \frac{\varepsilon_0 \varepsilon_l}{2d} \psi^2 \quad (1-5)$$

By replacing the above modified solid-liquid interfacial tension in the Young's equation (Equation (1-1)), Young-Lipmann's equation is achieved. This equation gives the relation between the actuated contact angle θ_V , non-actuated contact angle θ_0 , and the applied voltage ψ . The dependence of the contact angle with the applied voltage is generally described by this equation before contact angle saturation.

$$\cos \theta_V = \cos \theta_0 + \frac{\varepsilon_0 \varepsilon_l}{2d \gamma_{LG}} \psi^2 \quad (1-6)$$

Continuous electrowetting (CEW) has been introduced by Beni et al. [7]. They managed to actuate a droplet of a liquid metal by an external electric field along the channel. Lee and Kim [8] used CEW to make a liquid micromotor, which demonstrates continuous travel of a mercury drop along a round microchannel. They achieved a smooth rotary motion with a speed of 9.4 cm/s at a driving voltage of 10 V. Jackel et al. [9] used the physical basis of CEW to build an optical switch which has a very fast response time of 20 ms and a very low operating voltage of 1 V. Later, Washizu [10] fabricated arrays of microelectrodes on a substrate and used them in electrostatic transport and manipulation of liquid droplets. He experimentally demonstrated transport, deflection and mixing of droplets.

In order to move single droplets in a microchannel, an array of electrodes is required on one of the plates (top or bottom) while the other plate is considered as ground electrode. As shown in Figure 1-8, to make the droplet move inside the channel, the electrode just close to the leading edge of the droplet is switched on (darker electrode), while all the other electrodes are off. This results in a decrease in surface tension at the leading edge which consequently decreases the solid-liquid contact angle. At the trailing edge, since there is no variation in voltage contact angle remains unchanged. A net electrowetting force pointing toward the switched on electrode is generated because of the difference between leading edge and trailing edge contact angles. Continuous droplet movement is made possible by firing the electrodes on and off, successively.

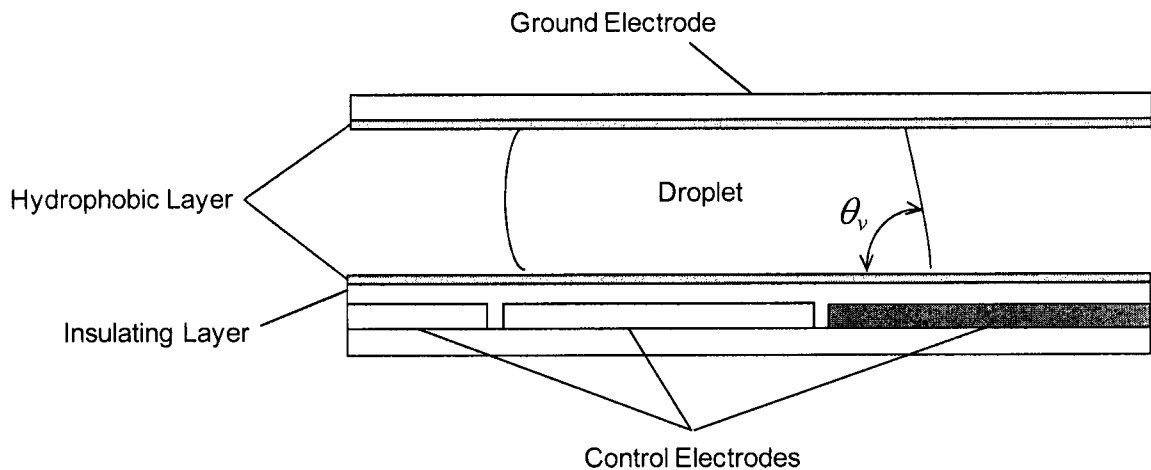


Figure 1-8 Droplet actuation via electrowetting (the darker electrode is fired)

Pollack et al. [11,12] showed the feasibility of electrowetting microactuation for the manipulation of aqueous droplets with different volumes. They investigated the effect of different parameters such as electrode pitch, channel height, applied voltage and surrounding media on the droplet movement. They could move the droplets with the

velocities as high as 10 cm/s with the actuation voltage of 60V. Such studies enabled the researchers to not only transport the individual droplets, but also dispense, mix, and split them. Paik et al. [13] Mixed microliters of liquid droplets by transporting the droplet along an electrode array. The effects of varying droplet aspect ratios (height/diameter) on linear-array droplet mixers have been studied later [14]. An optimal aspect ratio for four electrode linear-array was proposed which led to a mixing time of 4.6s. They reduced the mixing times to less than 3s using a two-dimensional array mixer. They also presented a split-and-merge mixer which resulted in a mixing time of less than 2s. Srinivasan et al. [15] presented an electrowetting-based microfluidic LOC platform for in vitro glucose measurement used in the clinical diagnostic applications. They have shown that there was no change in enzyme activity under electrowetting conditions. The feasibility of using an electrowetting-based digital microfluidic LOC for many more clinical diagnostics was later demonstrated [16]. Benefited from the spherical cap shape of the sessile droplets, several researchers [17,18,19] studied the concept of liquid lenses using droplets. The curvature of the interface and hence the focal length of the lens can be tuned by changing the droplet contact angle via electrowetting. This leads to the design of electrical optic systems with variable focal length.

Several recent studies have been engaged on improving the electrowetting phenomenon in order to have cheaper and easier actuation process. Heikenfeld and Dhindsa [20] have researched on the electrowetting in superhydrophobic structured surfaces. Substrate structures included silicon nanoposts and nanowires, carbon nanofibers and nanotubes, and polymer microposts. The reversibility of contact angle change has been demonstrated by means of liquid boiling or addition of a second non-polar liquid. Gong and Kim

[21,22] have adapted a multilayer printed circuit board (PCB) as the substrate for the first time. This new fabrication scheme is expected to lead to flexible, cheap and consequently disposable microfluidic systems. On the other hand, new and simple microfabrication methods for digital microfluidics are proposed recently which replace the photolithography [23]. Dielectric and hydrophobic layers were replaced by Saran TM wrap (polyethylene film) and commercial water repellents. Fabricated devices were successfully tested for droplet manipulation, merging and splitting. This fabrication method results in digital microfluidic systems with minimal costs. Yi and Kim [24] showed EWOD actuations on coplanar electrodes with an electrode-free cover plate or no cover plate. They demonstrated the successful moving, splitting and merging of micro drops in a parallel-plate or single-plate configurations. Such EWOD configuration can accommodate more sensing mechanisms from top of droplet and thus allows additional flexibility for system design.

Along with the experiments, analytical and numerical studies have been performed to clarify and strengthen the empirical results. Several researchers focused on derivation of equations for the droplet in the equilibrium condition. The equilibrium shape of a liquid drop under gravity and electrical fields has been described by Shapiro et al. [25] using an energy minimization concept. Numerical modeling of electrowetting has been performed using a shape inverse approach [26]. This model is based on total energy minimization to seek the droplet shape. It is numerically shown that the computed contact angles fit the predictions of Lippmann's equation only up to a critical applied voltage value. By increasing the voltage, an overestimation of the Lippmann prediction is observed. They also showed that the curvature increases sharply at the contact point while it remains

constant at the other points. Walker et al. [27] numerically showed that contact angle saturation and hysteresis are necessary to predict the correct shape and time scale of droplet motion. They implemented the saturation characteristics and a contact angle hysteresis model and showed that it better predicts the splitting experiment. A recent work has presented an analytical electromechanical model for calculating the forces acting on liquid droplets in a digital microfluidic device. The study explains the reason for movement of some particular fluids while some other fluids do not move under the same experimental conditions [28]. Nadim [29] developed the mathematical models to estimate the magnitude of forces and velocities achieved by electrowetting. These models consider electrowetting actuation of individual sessile drops on an array of electrodes. Zeng and Korsmeyer [30] analyzed the droplet electrohydrodynamics under EWOD and dielectrophoresis actuations. They used the simulations to show the capability of these methods for droplet generation and manipulation. In addition, they illustrated device operation in droplet translocation, droplet fusion, and droplet fission. Hong et al. [31] analyzed the electrowetting-based droplet motion with the presence of AC electric field around a droplet. Interestingly, the numerical results show the delay of the dielectric breakdown in the AC electrowetting, which could be related to the contact-angle saturation phenomenon.

Dolatabadi et al. [32] conducted numerical investigation of electrowetting in microchannels. They directly applied the actuated contact angle of the droplet in the VOF-based (volume of fluid) code without modeling the electric field. Even though their results were quite close to the experiments, a more precise model was still needed to calculate the contact angle. Another numerical simulation was carried out by Arzpeyma

et al. [33,34] to model behaviour of droplet under electrowetting actuation. The simulation included an algorithm to simultaneously calculate hydrodynamics and time dependant electric field in the domain. Their simulations used volume tracking technique and a static contact angle model to predict the droplet movement according to the calculated electric field. Another numerical study has been performed to verify the effect of adding the dynamic contact angle model by Keshavarz et al. [35]. They proved that the results obtained from dynamic wetting model well agree with the experimental data in literature.

Current work aims at the analysis of droplet behaviour when actuated with different electrode shapes. This study is jointly carried out by a numerical tool which contains a modified algorithm to predict the time and space varying electric field and the validating experiments. As the result, the effect of using a new electrode shape is illustrated by comparing several parameters such as droplet velocity, deformation, and contact angle.

1.4. ELECTRODE SHAPE

The electrode shape is one of the important parameters in electrowetting which has been rarely studied. The shape of the electrodes along with their dimensions could change the voltage distribution inside the channel. Any change in electric field affects the movement parameters and droplet deformation. A flat square electrode is a basic shape used in electrowetting applications (Figure 1-9(a)). This simple electrode shape is easy to fabricate and capable of moving the droplet.

The droplet diameter should be slightly larger than the length of the electrode to provide the overlap between the droplet and the adjacent electrode. With all the electrodes off, the

interface is unaffected. By applying a voltage to the electrode underneath the droplet, surface tension of the droplet will change and the droplet moves onto the charged electrode. The area of overlap between the droplet and electrode reaches to its maximum when the droplet completely moves on the electrode. Pollack et al. [11] reported a minimum droplet diameter to be actuated on a square flat electrode. They estimated the minimum droplet volume being able to move on the array by the volume of a cube formed on the base of the electrode between two parallel plates. This volume would be equal to the volume of a sandwiched droplet with the same channel height and the diameter of $= 2L/\sqrt{\pi}$ (L is the electrode length). Thus, they found an overlap of 6.4 % between the well-centered droplet and its adjacent electrode. As the droplet diameter exceeds this minimum value, it will be more difficult for the droplet to be centered relative to the electrode underneath it. As a result, droplet transport would be more difficult or even impossible on a simple flat electrode.

The interdigitated electrode shape has been introduced to provide the overlap between the consecutive electrodes (Figure 1-9(b)) [11]. This electrode shape reduces the sensitivity of the droplet movement to the position of droplet with respect to the electrode. It also makes the movement possible for a large range of droplet sizes. Such electrodes have zigzag sides which are placed one after the other to eliminate the apparent gap and provide overlap between the two adjacent electrodes.

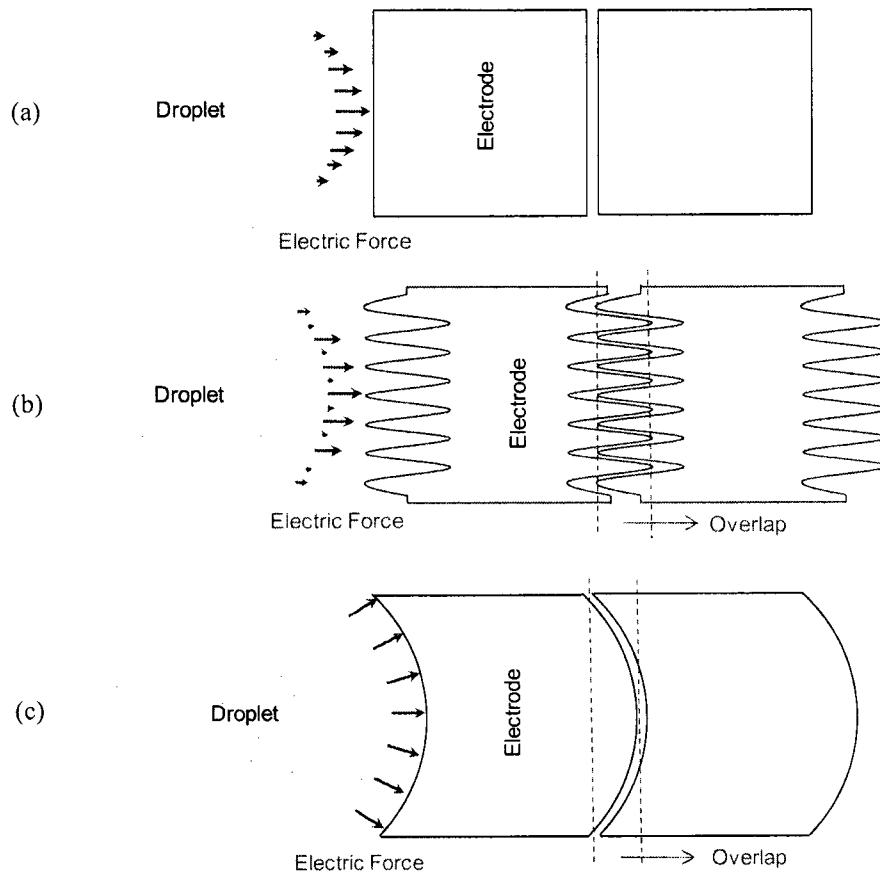


Figure 1-9 Different electrode shapes (a) flat (b) interdigitated (c) crescent

Various interdigitated electrodes are proposed by Lienemann et al. [2] with sinusoidal, rectangular or triangular spikes. Figure 1-10 shows these three different types of spikes. They calculated the potential energy for these three different interdigitated geometries with the Surface Evolver program [36]. The results have been compared with the results of a analytical geometric model. The model was based on the constant radius of contact line circle as well as constant area of liquid-air interface. They finally recommended the use of sinusoidal interdigitated shape in electrowetting experiments.

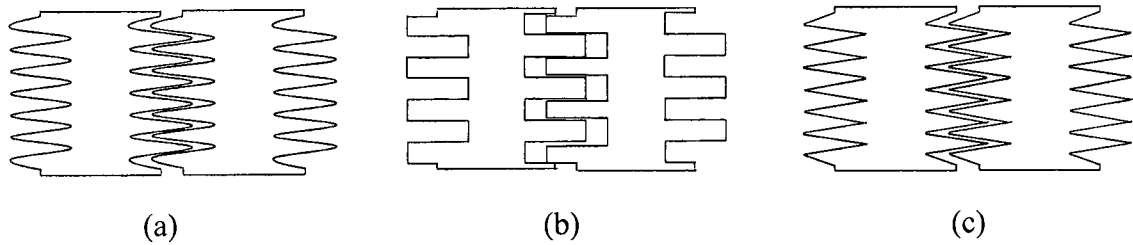


Figure 1-10 Interdigitated electrodes (a) sinusoidal (b) rectangular (c) triangular

Although the interdigitated electrode has been widely used to provide overlap between the electrodes, it has its own shortcomings. This electrode shape is very difficult to layout and fabricate due to its complex shape. This complexity in geometry makes the system analysis and modeling to be a challenging task. Moreover, the insulator is easily subject to voltage breakdown in the insulator between the gaps because of the sharp voltage contours created. Other disadvantage of both flat and interdigitated electrodes is the force applied on the meniscus of droplet. As illustrated in Figure 1-9 (a,b), the forces are applied in a non-uniform way which results in the excessive droplet stretching.

In this work, a new crescent-shaped electrode has been introduced which provides overlapping feature (Figure 1-9(c)). More importantly, this electrode shape is designed to preserve the droplet shape by minimizing the stretching of the droplet and having a more uniform distance between the leading edge of the droplet and the edge of electrode. In addition, compared to the interdigitated electrodes, the crescent electrode results in less complexity and fabrication cost. It also reduces the risk of having voltage breakdown of the insulator. This promising electrode shape is expected to facilitate device fabrication and droplet actuation in electrowetting.

1.5. OBJECTIVES

The objective of this work is to investigate the effect of electrode shape in droplet behaviour under electrowetting actuation. For this purpose, both numerical and experimental approaches are followed in this thesis. In the numerical study, a new algorithm is applied on the existing code to calculate the interfacial voltage to better estimate the droplet deformation and movement at the onset of actuation which is more of interest in this work. Moreover, the effect of dynamic contact angle is added and compared with the static model. Experimental part focuses on the movement and deformation of droplet at onset of actuation for flat and crescent electrodes. The experiments are mainly performed to validate the modified numerical results. Ultimately, this thesis proposes the use of a new electrode shape to achieve higher velocities, lower deformation and easier actuation in electrowetting-based digital microfluidics systems.

1.6. THESIS STRUCTURE

The next chapter discusses the required mathematical formulations which explain the electrowetting phenomenon; the flow governing equations along with the electric field equation, the numerical modifications made to the code and the dynamic contact angle implementation. Chapter 3 gives a complete explanation on the procedure of sample fabrication and preparation as well as experimental setup needed to perform the tests. In the last chapter, a combination of numerical and experimental results is presented and the conclusions will highlight the importance of these results.

2. NUMERICAL TECHNIQUE

This chapter is dedicated to explaining the equations which govern the droplet motion via electrowetting. These equations include flow governing equations, electric potential equations, and dynamic contact angle equations. Herewith, the boundary and initial conditions and the applied numerical schemes are discussed.

2.1. DROPLET DYNAMICS

The flow is assumed to be laminar, incompressible and Newtonian where viscosity, density, and surface tension are constant.

2.1.1. Governing Equations

Conservation of mass and momentum is presented by following equations,

$$\nabla \cdot \vec{V} = 0 \quad (2-1)$$

$$\frac{\partial \vec{V}}{\partial t} + \nabla \cdot (\vec{V}\vec{V}) = -\frac{1}{\rho} \nabla p + \frac{1}{\rho} \nabla \cdot \tilde{\tau} + \vec{g} + \frac{1}{\rho} \vec{F}_b \quad (2-2)$$

where \vec{V} is the velocity vector, p the pressure, ρ the liquid density, $\tilde{\tau}$ the shear stress tensor, \vec{g} gravitational acceleration, and \vec{F}_b any body forces (per unit volume) applied on the fluid. For a Newtonian fluid, shear stress is given by,

$$\tilde{\tau} = \mu \left(\nabla \vec{V} + (\nabla \vec{V})^T \right) \quad (2-3)$$

where μ represents the dynamic viscosity of liquid.

The flow equations are written in the Eulerian frame of reference. The solution of these equations should be coupled with a method to track the deforming liquid-gas interface. Therefore, a piecewise linear volume tracking algorithm is implemented which uses a scalar function of f as its variable parameter.

$$f = \begin{cases} 1 & \text{within the liquid phase} \\ 0 & \text{outside of the liquid} \end{cases}$$

The advection equation read as,

$$\frac{\partial f}{\partial t} + (\vec{V} \cdot \nabla) f = 0 \quad (2-4)$$

A 3D code developed by Bussmann et al. [37,38] is used which is based on the RIPPLE model [39,40]. RIPPLE is a 2D fixed-grid Eulerian code developed specifically for free surface flows with surface tension. Governing equations are discretized on a Cartesian mesh by applying MAC, Marker and Cell method. In this method, velocities are defined at the center of cell faces while the pressure is specified at the cell center [41,42,43].

Approximate reconstruction of the interface and evaluation of fluid fluxes across cell surfaces are two steps of volume tracking schemes. In this work, a piecewise linear interface calculation (PLIC) approach has been applied [44]. Depending on the amount of volumetric parameter of $f_{i,j,k}$ and direction of $\hat{n}_{i,j,k}$, the interface is reconstructed by locating a plane within each interface cell. In 2D, this interface is a line crossing the cell where in 3D it becomes a polygon. The position of the interface and the velocities at the cell faces are used to calculate the fluid flux. Exact liquid interface, 2D volume fraction field and fluid flux are shown in Figure 2-1.

To impose a boundary condition to the equation of pressure, we consider a general boundary condition expression which must be satisfied at the moving interface of fluid 1 and 2 [45] (1 and 2 represent the liquid and gas phase, respectively).

$$(p_1 - p_2 - \gamma\kappa)n_i = (\tilde{\tau}_{1,ik} - \tilde{\tau}_{2,ik})n_k + \frac{\partial \gamma}{\partial x_i} \quad (2-5)$$

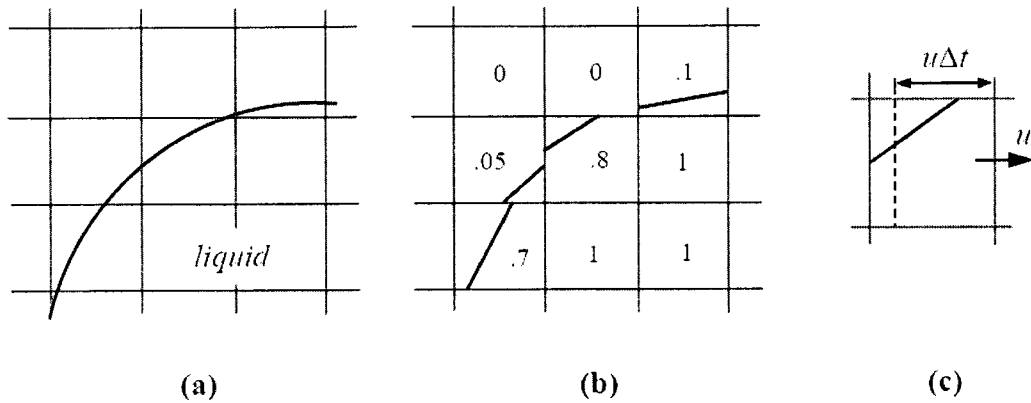


Figure 2-1 Volume fraction advection in 2D (a) an exact liquid interface, (b) corresponding f_{ij} and the associated planar interfaces, (c) with u positive, the region to the right of the dashed line is advected into the neighboring cell [37].

p_1 and p_2 are the pressures on either side of the interface, n_i is a component of the unit normal \vec{n} directed into fluid 1, γ is the interfacial surface tension, and κ is the local curvature which reads as,

$$\kappa = \frac{1}{R_1} + \frac{1}{R_2} \quad (2-6)$$

where R_1 and R_2 represent the principal radii of curvature. Applying zero shear stresses and constant surface tension, Equation (2-5) is simplified into the Laplace equation. This equation defines the surface tension-induced pressure jump across the liquid-gas interface.

$$\Delta p = p_l - p_g = \gamma\kappa \quad (2-7)$$

Surface tension force is calculated according to the following equation.

$$\vec{F}_{ST}(\vec{x}) = \gamma \int_S \kappa(\vec{y}) \hat{n}(\vec{y}) \delta(\vec{x} - \vec{y}) dS \quad (2-8)$$

where \hat{n} represents a unit normal to the interface directed into the liquid and δ is the Dirac delta function. The integration is performed over the area of free surface S . Geometric characteristics of the surface, κ and \vec{n} , may be written in terms of f .

$$\kappa = -\nabla \cdot \hat{n} \quad (2-9)$$

$$\hat{n} = \frac{\nabla f}{|\nabla f|} \quad (2-10)$$

As proposed in the Continuous Surface Force (CSF) model by Brackbill et al. [46], surface tension is converted to an equivalent body force and inserted in the equation of conservation of momentum (Equation (2-2)) by the term \vec{F}_b instead of the direct application of pressure boundary condition (Equation (2-7)) as the boundary condition. While considering finite approximation of δ in Equation (2-8), surface tension force on the interfacial cells should be applied in a way that the two sides of the interface experience similar surface tension –induced acceleration.

To apply the contact angle constraint on the walls, the surface tension force is calculated at the cells adjacent to the solid substrate to apply the contact angle constraint on the walls. Contact angle is a thermodynamic property of the matter and is defined by surface

tension forces. This angle is applied in the code by defining the direction of unit normals in the liquid cells adjacent to the solid substrate.

2.1.2. Boundary and Initial Conditions

All the governing equations are subject to boundary conditions applied at solid interfaces, at symmetry boundaries, and at the fluid free surface. A unit vector \hat{n}_\perp is defined as normal to a solid boundary, and a unit vector \hat{t}_\perp is defined as tangential to the boundary. Fluid velocity obeys the no-slip and no-penetration conditions.

$$\vec{V} \cdot \hat{t}_\perp = 0 \quad (2-11)$$

$$\vec{V} \cdot \hat{n}_\perp = 0 \quad (2-12)$$

Zero pressure gradient is also imposed across the solid boundary.

$$\nabla p \cdot \hat{n}_\perp = 0 \quad (2-13)$$

To reduce the size of a specific problem and number of calculations, symmetry boundaries are implemented for planar symmetry. Symmetric boundaries are shown with parallel sign subscript. The fluid velocity satisfies slip and no-penetration conditions all along the symmetry boundary.

$$\nabla(\vec{V} \cdot \hat{t}_\parallel) \cdot \hat{n}_\parallel = 0 \quad (2-14)$$

$$\vec{V} \cdot \hat{n}_{\parallel} = 0 \quad (2-15)$$

Across the boundary, the gradients of p and f are inherently zero.

$$\nabla p \cdot \hat{n}_{\parallel} = 0 \quad (2-16)$$

$$\nabla f \cdot \hat{n}_{\parallel} = 0 \quad (2-17)$$

Zero shear stress is the boundary condition which is applied at the fluid free surface:

$$\tilde{\tau}_s = 0 \quad (2-18)$$

Zero tangential stress imposed at the free surface can be explained by means of three types of velocities: tangential velocities, new fluid velocities, and external velocities. Figure 2-2 shows a 2D example. Velocity at faces between two empty cells next to interfacial cells is defined as tangential velocity. The velocity between two interfacial cells which were empty before the latest time step is called new fluid velocity. The velocity is considered to be equal to the nearest velocity within the fluid. External velocities are velocities at cell faces between an interfacial and an empty cell. The local divergence $\nabla_{i,j,k}$ of velocity should be zero.

Since the surface tension force has already been applied in the Navier-Stokes equation, the boundary condition of pressure reduces to,

$$p_s = 0 \quad (2-19)$$

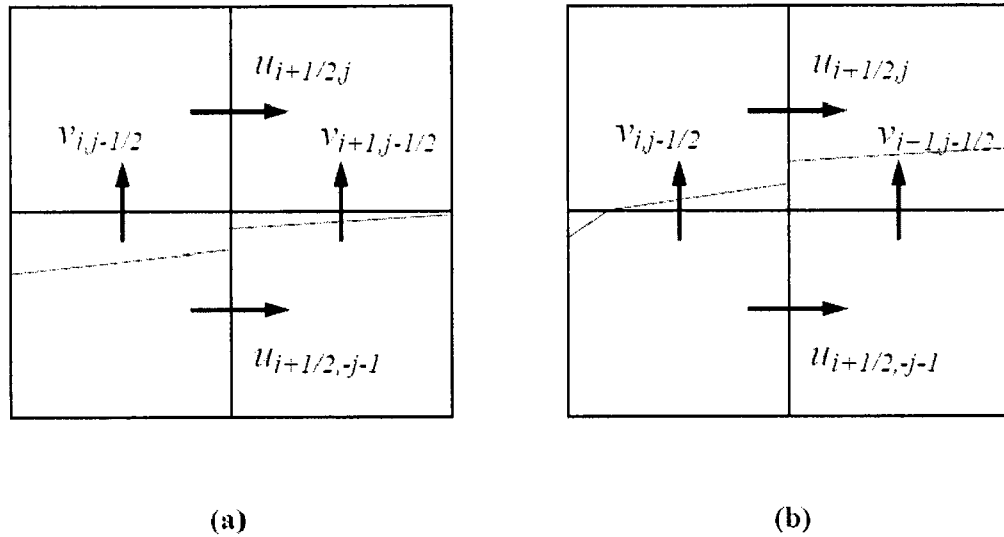


Figure 2-2 Free surface boundary conditions in 2D (a) tangential velocity (b) new fluid velocity; for

$$\text{both cases } u_{i+\frac{1}{2},j} = u_{i+\frac{1}{2},j-1} \quad [37].$$

To evaluate surface tension force equation (Equation (2-8)) it is necessary to define \hat{n} at the contact line, where a free surface meets a solid surface. For a sessile droplet sitting on a solid substrate, $\theta = \theta_e$ is a thermodynamic property of the system at equilibrium condition. This angle is the one expressed in Young's equation (Equation (1-1)) and is the angle between the solid-liquid and liquid-gas surface tensions. The wettability of the liquid on the solid surface is also defined by this angle.

The computational domain was discretized into Cartesian cubic elements of side of 20 and 50 μm . Simulations done with these two mesh sizes did not show significant improvement in favor of the finer mesh in calculated velocity for different voltages. Therefore, a mesh size of 50 μm was used in the simulations to reduce the computational time.

2.1.3. Timestep Restrictions

To gain a stable solution, there are some restrictions imposed on the timestep by explicit evaluation of the convective, viscous, and surface tension terms. Momentum cannot be advected more than a single cell. This implies that the Courant number should satisfy the following condition,

$$\max \left[\frac{|u_{i,j,k}| \Delta t}{\Delta x_i}, \frac{|v_{i,j,k}| \Delta t}{\Delta y_j}, \frac{|w_{i,j,k}| \Delta t}{\Delta z_k} \right] < 1 \quad (2-20)$$

This condition is also required by the volume tracking algorithm, because volume can only be advected into the neighbouring cells. In the same way, momentum cannot diffuse more than one cell in a single timestep,

$$\Delta t < \frac{\rho}{\mu} \cdot \min \left[\frac{(\Delta x_i)^2 (\Delta y_j)^2}{(\Delta x_i)^2 + (\Delta y_j)^2}, \frac{(\Delta x_i)^2 (\Delta z_k)^2}{(\Delta x_i)^2 + (\Delta z_k)^2}, \frac{(\Delta z_k)^2 (\Delta y_j)^2}{(\Delta z_k)^2 + (\Delta y_j)^2} \right] \quad (2-21)$$

And ultimately, as the timestep should be small enough to resolve the propagation of capillary waves which cannot travel more than a cell width, Brackbill et al. [46] derived following condition,

$$\Delta t < \sqrt{\frac{\rho}{4\pi\pi}} \cdot \min \left[(\Delta x_i)^{\frac{3}{2}}, (\Delta y_j)^{\frac{3}{2}}, (\Delta z_k)^{\frac{3}{2}} \right] \quad (2-22)$$

Time step for any numerical cycle is the minimum value resulting from any of these three relations.

2.2. ELECTRIC POTENTIAL

In order to model the electrowetting phenomenon, the electric potential resulted from a voltage applied across the channel should be calculated throughout the entire domain. In this section, first the derivation of the mathematical equation is presented. Then, the previous algorithm of applying voltage on interfacial cells and consequently in the entire domain is explained. This algorithm has been modified and improved to better estimate the voltage distribution in the current study. This modification is explained afterwards.

The electric field inside the domain is formulated from Maxwell's first equation. Gauss's law says that the total electric flux through a closed surface is equal to the charge enclosed in the domain.

$$\oint_s \vec{D} \cdot d\vec{s} = \int_{Vol} \rho_v dV \xrightarrow{\text{to satisfy divergence theorem}} \text{div}\vec{D} = \rho_v \quad (2-23)$$

Where \vec{D} is the electric flux density and ρ_v is the volumetric electric charge density.

The relation between the electric flux and the electric field can be shown as,

$$\vec{D} = \epsilon_0 \epsilon_r \vec{E} \quad (2-24)$$

Where ε_0 is the permittivity of free space and ε_r is the relative permittivity of the insulating layer. Thus, $\varepsilon = \varepsilon_0\varepsilon_r$ represents the dielectric constant of the insulating layer.

The electric potential and the electric field are related as,

$$\vec{E} = -\vec{\nabla} \psi \quad (2-25)$$

By applying *div* operator to both sides of Equation (2-25) and using Equations (2-23) and (2-24), the differential equation to calculate the electric potential inside the domain is obtained. In fact, the equation is a Poisson equation which reads as follows.

$$\nabla^2 \psi = -\frac{\rho_v}{\varepsilon} \quad (2-26)$$

The well-known Laplace equation is achieved when there is no net electric charge density in the system.

$$\nabla^2 \psi = 0 \quad (2-27)$$

As electrowetting deals with rearranging the surface charges, there is no extra charge added or removed from the system. Therefore, the Laplace equation with proper boundary conditions gives the electric field distribution in the domain.

The electric field equation along with the flow equations are solved simultaneously to capture the effects of the imposed electric field at each timestep throughout the computational domain. Laplace Equation (2-27) is solved using a second order finite difference equation. The discretized version of Equation (2-27) in space is,

$$\psi_{i,j,k} = \frac{1}{6} [\psi_{i+1,j,k} + \psi_{i-1,j,k} + \psi_{i,j+1,k} + \psi_{i,j-1,k} + \psi_{i,j,k+1} + \psi_{i,j,k-1}] \quad (2-28)$$

The converged solution of the Laplace equation is obtained using Gauss–Seidel iterative method with a maximum residual of 10^{-6} . After solving the electric field at each node, the Young-Lippmann's equation (Equation (1-6)) is used to find the actuated contact angle.

$$\theta_{i,j,k}^{new} = \cos^{-1} \left[\cos \theta_0 + \frac{\epsilon_0 \epsilon}{2d\gamma_{LG}} (\tilde{\psi}_{i,j,k}^n)^2 \right] \quad (2-29)$$

In Figure 2-3 (a), there is no electric potential present in the domain. The contact angle has decreased in Figure 2-3 (b) based on the effective interfacial voltage, $\tilde{\psi}_{i,j,k}$. This yields a change in the direction of the normals which then affects the value of the surface tension force.

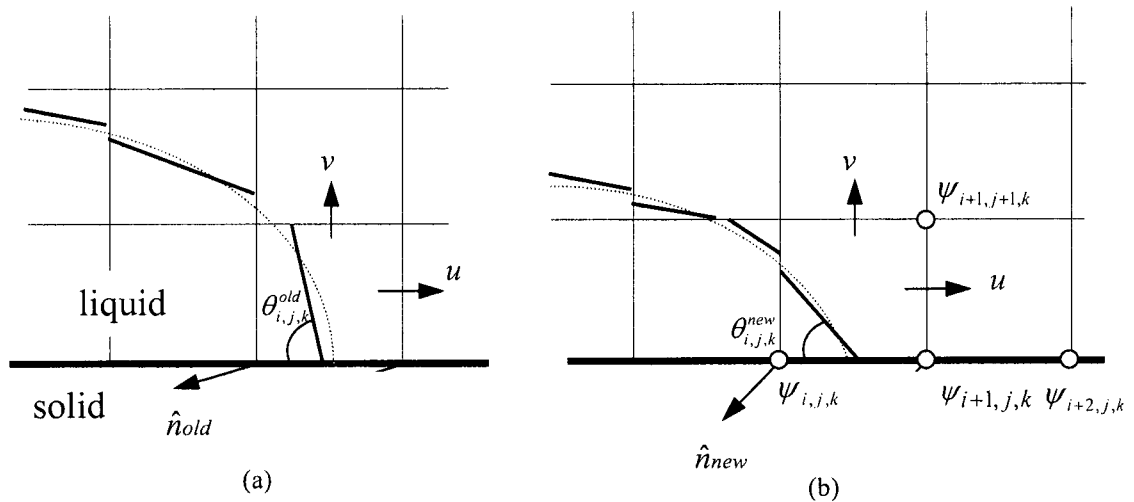


Figure 2-3 Contact angle change (a) before applying the voltage (b) after applying the voltage [33]

In general, there are three different types of computational cells throughout the domain regarding the applied voltage; cells with $f=0$ (cells with no liquid), cells with $f=1$ (cells fully occupied by liquid), and cells with $0 < f < 1$ (interfacial cells). For the cells with $f=0$, the electric potential is directly calculated by the Laplace equation. The voltage in the cells with $f=1$ is zero. For the interfacial cells, the effective voltage may be calculated based on the cell volume fraction. For example, for a cell with $f=0.5$, the effective voltage is $0.5 \times \psi_{i,j,k}$. Although, this weighing method is numerically straight forward and easy to implement, it does not represent the physics governing the droplet wetting. Indeed, the effective voltage of each interfacial cell is the voltage of the empty portion of that cell. Therefore, the contact line can experience no voltage on one side and voltage calculated by the Laplace equation on the other side. To overcome this issue, Equation (2-30) was previously applied at the interface as the effective voltage on the contact line.

$$\tilde{\psi}_{i,j,k} = \frac{(\psi_{i+2,j,k} + \psi_{i+3,j,k})}{2} \quad (2-30)$$

Since the Laplace equation is not solved in substrate cells and the electric potential for the cells filled with liquid is considered zero, the substrate cells have the voltage of either zero, initial value or the electrode voltage. According to Equation (2-30), the effective voltage in each interfacial cell on the substrate is based on the voltage of the second and third cells in front. Using this scheme, three amounts of voltages are used for all the cells on the substrate depending on their relative position to the electrode cells as shown in Figure 2-4. Droplet contact line begins to feel half of the electrode voltage when the droplet leading edge is still three cells away from the first point of (Figure 2-4 (a)).

Figure 2-4 (b,c,d) show the overestimation of the effective voltage in three different distances of droplet from the electrode. Along with this unreasonable voltage implementation, the Laplace equation previously used zero volts in cells full of fluid as a boundary condition. Because of this boundary condition, the voltages calculated in the rest of computational cells were less than what they could be without this boundary condition. Physically, the voltage applied on the contact line is not affected by the zero voltage inside droplet.

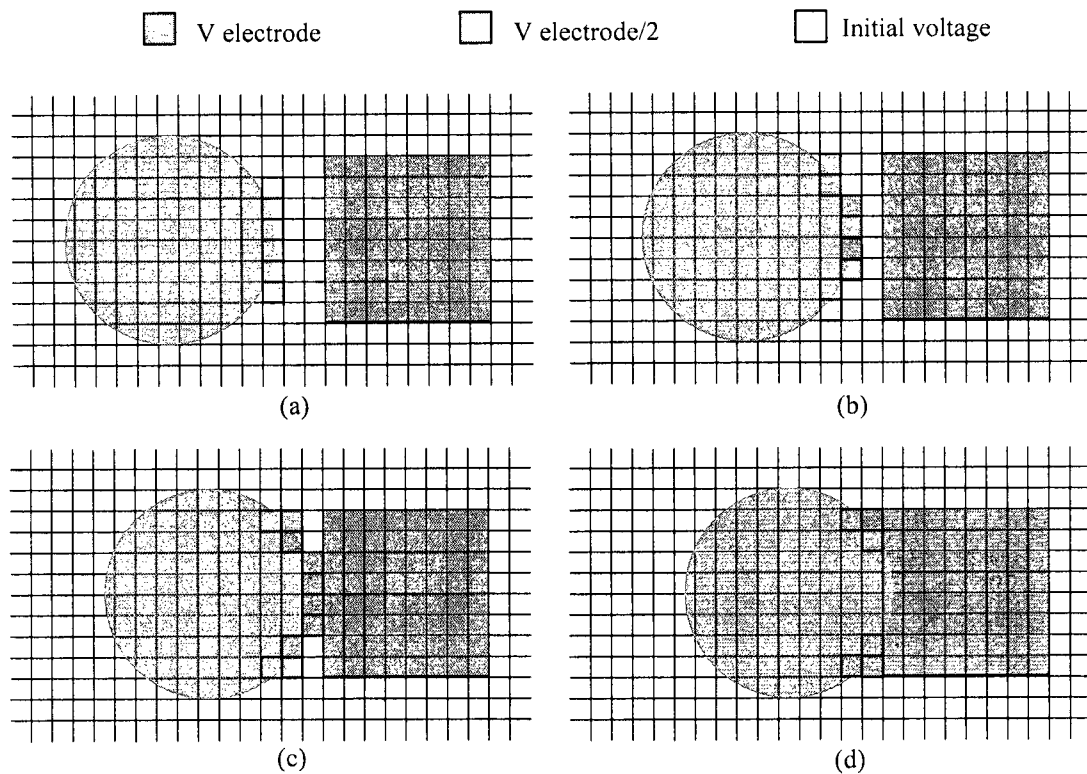


Figure 2-4 Effective interfacial voltage on substrate cells using the cell averaging method.

In this work, another scheme is presented and applied to calculate the effective interfacial voltage. .Figure 2-5 shows the schematic of voltage contours on the substrate surface

obtained by the new method. In this method, first the Laplace equation is solved all over the domain with the only boundary condition of the electrode voltage. Solving the Laplace equation, a smooth distribution of voltage in the entire domain is obtained originating from the electrode cells shown in Figure 2-5(a). Then, voltages in all the cells with volume fraction of 1 are set to zero (Figure 2-5(b)). Thus, there is no need to separately calculate the voltage for interfacial cells of substrate level, because they already have a value computed by the Laplace equation. A detailed interfacial voltage distribution on substrate surface is illustrated in Figure 2-5(c).

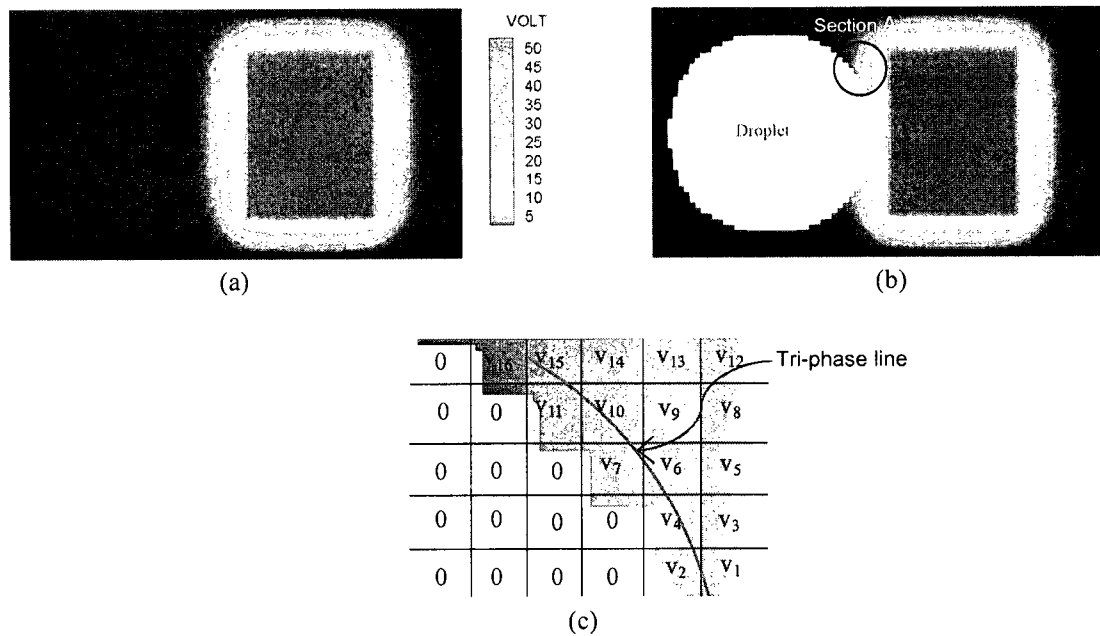


Figure 2-5 Schematic of voltage distribution using the new voltage implementation (a) before defining droplet location (b) after placing the droplet (c) a larger view of section A A

The electric field distribution in the domain changes with time and space. First, the electrodes are switched on and off sequentially and second, the droplet position in the

domain changes the electric field. As moving boundary condition, the powered electrode location changes when another electrode is switched on. Since the top electrode is grounded, the potential for the conductive droplet is zero. Thus, the moving droplet imposes a series of zero potential moving cells.

2.3. DYNAMIC CONTACT ANGLE

Studies of the moving of droplet often use a static contact angle model disregarding this fact that contact angle at the tri-phase contact line shows dynamic behavior. Using this simplification may decrease the accuracy of the simulation in most cases. In static modeling of our simulations, the droplet contact angle is calculated through Young-Lippmann's equation. The voltage in each interfacial cell of substrate surface is calculated by the Laplace equation. This voltage is inserted into Young-Lippmann's equation and the change of contact angle is obtained. Therefore, by applying static contact angle model, only the effect of voltage is applied in calculation of actuated contact angle. However, in real physical phenomenon, after the initial actuation, contact angle is no longer the initial static value.

The accurate mechanism of dynamic wetting and dewetting is not completely understood yet. Blake [47] has posed one of the most appropriate and realistic approaches to explain the experimental observations and clarify the underlying physical mechanism, i.e. molecular-kinetic theory. Using this approach, the molecular details of wetting are clarified as experimental observations reveal that the contact line motion takes place on a microscopic molecular scale. Contact line motion is shown as a series of discrete jumps on the molecular scale while dissipating energy. Although energy dissipation occurs at

the molecular level, its effects can be reflected on the macroscopic level. Another advantage of Blake's model is its validity for both advancing and receding contact lines while the empirical models are valid only for advancing contact line [48]. Herewith, electrowetting model is improved by introducing dynamic contact angle model employing molecular-kinetic theory suggested by Blake [47].

Dynamic contact angle is one of the most important parameters in wetting of droplet during movement. Droplet Contact angle changes from its static value at equilibrium to dynamic one which can be either advancing or receding. The advancing angle is the contact angle when the tri-phase line is moving over and wetting the surface, while the receding angle is the contact angle when the tri-phase line is withdrawn over a pre-wetted surface. Advancing contact angle is larger than equilibrium contact angle and the receding contact angle is smaller than equilibrium contact angle [49,5].

The contact line motion is influenced by magnitude and direction of the contact line velocity. Using molecular-kinetic theory, the contact line velocity is determined by k^0 and λ which are the equilibrium frequency of the random molecular displacements and the average distance of each displacement, respectively. These displacements occur at the adsorption sites on the solid surface during dissipative and thermodynamically irreversible processes. The out of balance surface tension (Equation (2-31)) can drive bulk flow to move the contact line [47].

$$F_w = \gamma_{LG}(\cos\theta_s - \cos\theta_D) \quad (2-31)$$

where θ_S and θ_D are static and dynamic contact angles, respectively. Combining this idea with Frenkel-Eyring [50] activated rate theory of transport in liquids leads the following relationship introduced by Blake [47],

$$U = 2k^0 \lambda \sinh[\gamma_{LG} (\cos \theta_S - \cos \theta_D) \lambda^2 / 2k_B T] \quad (2-32)$$

where k_B and T are the Boltzmann constant and absolute temperature, respectively. Several expressions for k^0 , characteristic frequency, based on thermodynamic arguments have been proposed to date. If the argument of *sinh* function is adequately small, velocity of the contact line can be determined as follows [47].

$$U \approx k^0 \lambda^3 \gamma_{LG} (\cos \theta_S - \cos \theta_D) / k_B T = \gamma_{LG} (\cos \theta_S - \cos \theta_D) / \xi \quad (2-33)$$

Where $\xi = k_B T / k^0 \lambda^3$ is the coefficient of wetting line friction; k^0 , λ , and, ξ are determined experimentally. The experimental value of ξ has been reported in few studies. Experimental studies by Ren et al. [51], Wang and Jones [52], Chen and Hsieh [53], Decamps and Coninck [54], showed that the assumption of small argument for *sinh* is a valid assumption for the case under investigation.

Equations (2-31) to (2-33) are utilised to introduce dynamic effects of contact line motion on droplet actuation in this study. Figure 2-6 illustrates the steps taken in the numerical algorithm. As tri-phase contact line velocity is calculated, contact angle is computed using molecular-kinetic theory. The calculated dynamic contact angle is then substituted in the Young-Lippmann's equation to obtain the final contact angle. This new contact angle has the effects of both dynamic contact angle and electric field. The velocity half

cell above the contact line on the solid surface has been used as the tri-phase contact line velocity. Regarding the superimposition of electrical and dynamic effects in the calculation procedure, Blake et al. [55] included electrical effects in molecular-kinetic theory. Having independently applied dynamic wetting and electrostatic effects, they proved the agreement between experimental observations and the results of the combined model in predicting the electrowetting phenomenon. Secondly, calculation of contact angle using molecular-kinetic theory depends on the friction factor of the surface.

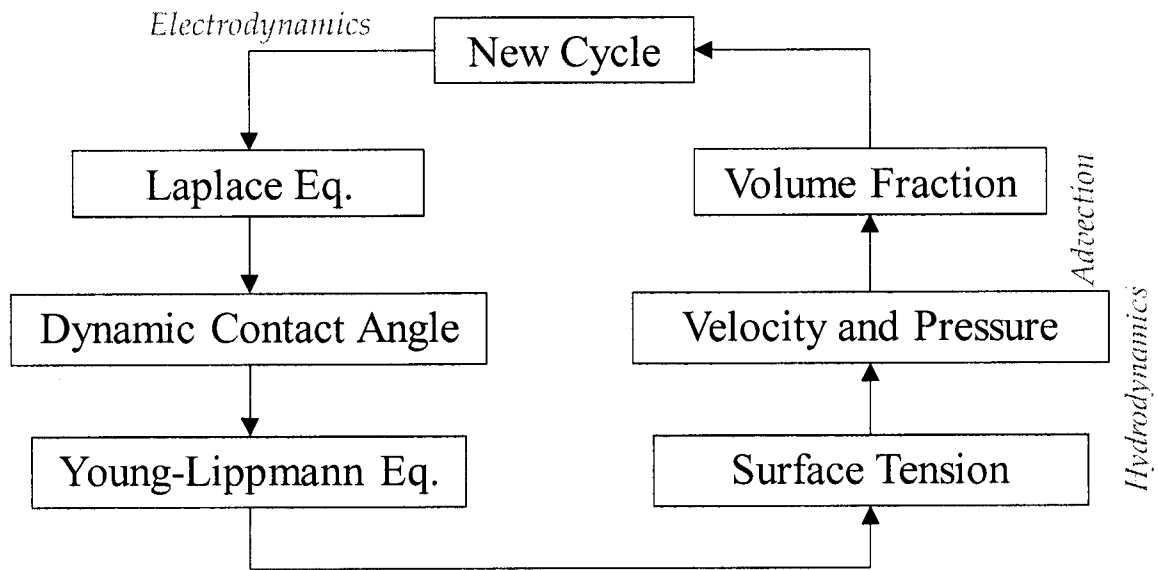


Figure 2-6 The numerical algorithm applied in this study

3. EXPERIMENTAL APPROACH

This chapter describes the complete procedure for microfabrication and preparation of the samples and describe the test rig which was used to perform the droplet transport experiments. A major component of this work includes the validation experiments to find the detailed information on electrowetting-based droplet actuation.

3.1. MICROFABRICATION

Microfabrication describes a collection of processes and technologies utilized in making miniature structures. This term has been originally used in microelectronics technology. The micro patterns are usually made on silicon wafers; however, other kinds of substrates such as glass are also in use. In our experiments, the electrodes were fabricated on glass

slides. Another electrode-coated glass slide is placed on top of the sandwiched droplet which acts as the ground electrode. Figure 3-1 shows the coating arrangement of the substrates used in the experiments. . The electrowetting chips were fabricated using standard microfabrication techniques at McGill Nanotools Microfab laboratory. For printing the electrode patterns on the glass, optical microlithography is used to selectively remove parts of a thin film of the electrode. Ultraviolet light transfers a specific pattern from a photomask to a photoresist on the substrate.

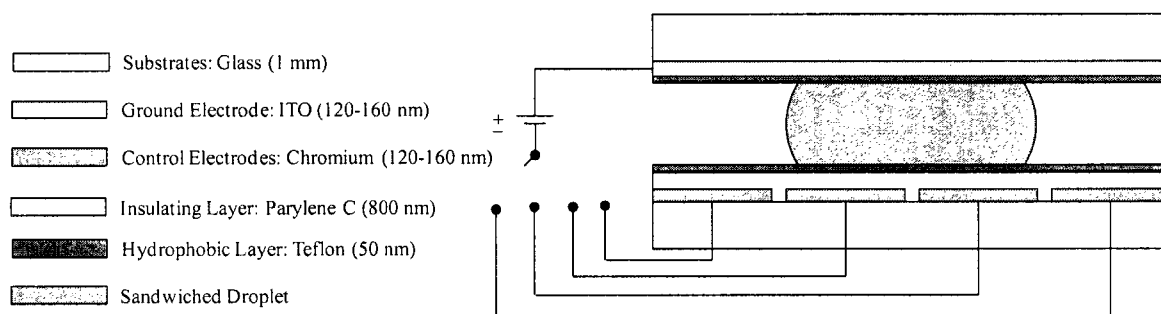


Figure 3-1 Schematic of microchannel plates with different layers of coatings

3.1.1. Photomask

Fabrication procedure starts with designing the mask. Basically, a photomask is a transparent glass with a specific chromium pattern. It allows the light to shine through non-chromium patterns in order to proceed with etching process of those patterns. The mask was designed in AUTOCAD[®] 2007 software according to the specification of photolithography apparatus [56]. The designed mask was fabricated at FineLine Imaging Company located at Colorado, USA. As there were patterns as small as 5 microns on the mask, it was printed with highest resolution technology. Figure 3-2(a) shows the printed

mask and Figure 3-2(b) shows a magnified section of the mask where the chromium parts will shape the electrodes. This mask enables us to do simultaneous microlithography for 6 samples of 3 by 1 inches.

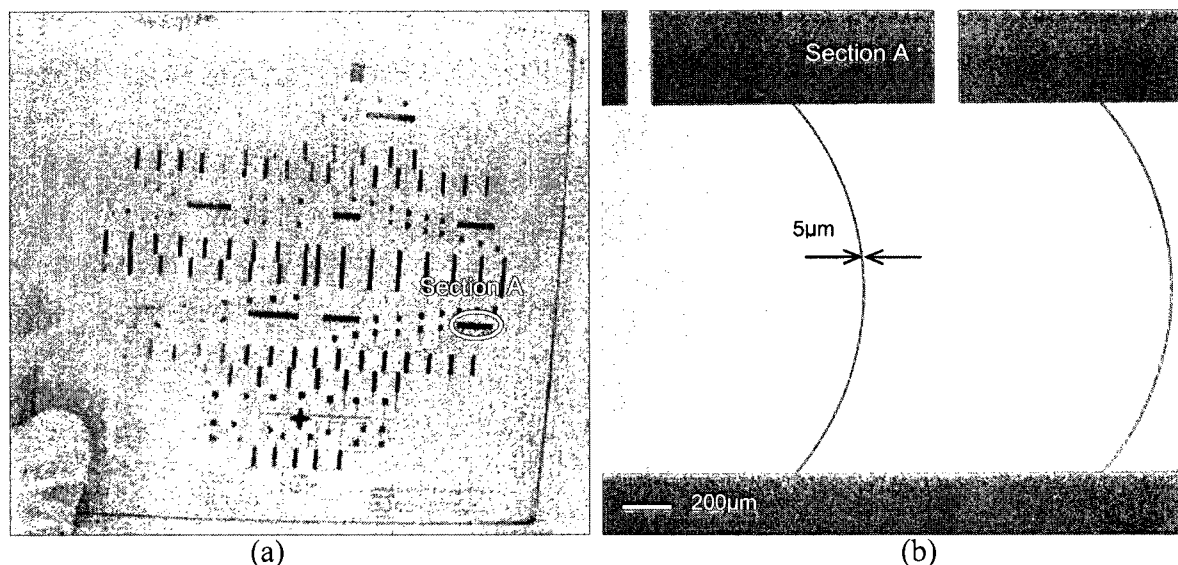
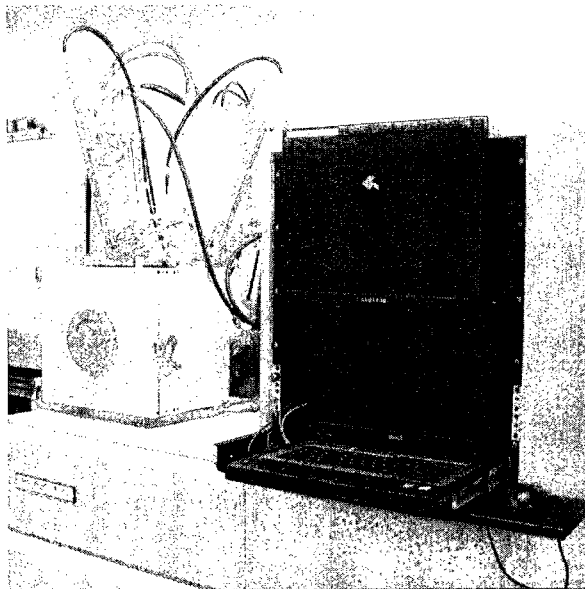


Figure 3-2 Top view of designed mask (a) printed mask (b) magnified image of section A

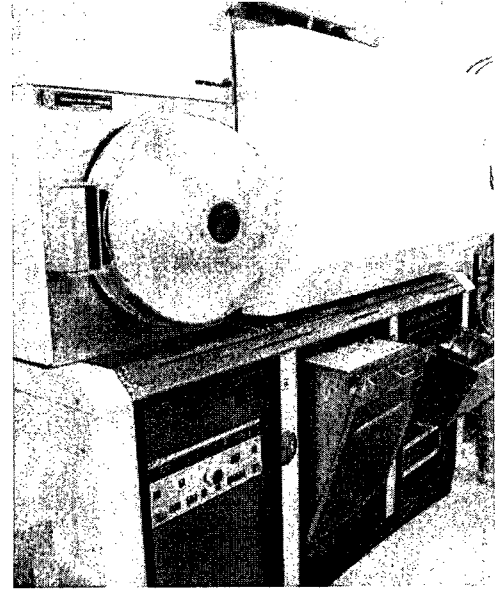
3.1.2. Electrode Layer

The transparent indium tin oxide (ITO) conductor as ground electrode has been deposited using reactive sputtering. The transparency of this layer helps to visualize the droplet motion from top. In this method, ITO film is formed by chemical reaction between the target material and a gas inside the vacuum chamber of Denton RF sputtering machine [57,58]. This machine is shown in Figure 3-3 (a). By varying the gas pressure, the composition of the film can be controlled. Since the conventional profiler cannot be used for transparent samples, NanoSpec/AFT 2100 has been utilized for measuring the thickness of ITO film. Because there is no recipe for the ITO film on the glass substrate, Nitride on silicone oxide recipe was used instead (because the refractive index of ITO

and Nitride are almost the same). Thus, a silicone oxide wafer was also coated with ITO by the same program used for the glass substrate. The measurements gave us an average thickness of 150 nm for the ITO layer. Another parameter that has to be considered is the uniformity of the coating. A uniform layer of ITO would have the same color all across the surface and it also shows the same number for resistivity. Considering these two parameters, i.e. color and resistivity, a uniform layer of ITO was finally obtained with an average resistivity of 11.5 Ω .m. The resistivity has been measured using a four-point prob.



(a)



(b)

Figure 3-3 Electrode deposition machines (a) Denton RF (b) MRC 603

The control electrode on the bottom plate can be made of any thin metal film. There are few requirements for this film such as conductivity and good adhesion to the glass. However, darker and less shiny layers of electrodes on the bottom plate provide clearer

pictures and give us the ability to check the exact location of droplet with respect to the electrode. On the other hand, it is important to use a transparent material for the top-plate conductor in order to be able to visualize the transport phenomenon.

The samples are plain pre-cleaned microscope glass slides with an area of 75×25 mm (3×1 inches) and the thickness of 1 mm. The slides should be as clean as possible to increase the quality and adhesion of the coating layers. The simplest way to remove the mineral residues from any substrate is using isopropanol (IPA) solvent. If there are more residues on the substrate, one might use the ultra-sonification bath in specific temperature for a specific time to improve and speed up the cleaning procedure [59].

A sputtering machine (MRC 603) [60], shown in Figure 3-3 (b), has been used to sputter chromium on the bottom glass slide. Sputtering is a physical vapour deposition method for depositing films. In this method, sputtered ions are ejected from the target and deposit on the substrate placed in the chamber filled with an inert gas such as argon. The coating procedure has been tried several times to get the appropriate thickness for the chromium layer which is 150 nm. Tencor P1 Profilometer [61] was used to measure the thickness of chromium on the glass surface. This measurement tool has a stylus which moves while touching the surface for a specified distance and specified contact force and it measures the height variations across the surface.

The control electrodes are formed by patterning the deposited chromium layer through the following steps,

1. Soak samples in IPA and rinse them with IPA

2. Dry samples with pressurized N₂ gas
3. Spin photoresist on samples (S1813 positive photoresist)
4. Soft bake (115°C for 7 minutes)
5. Alignment and exposure
6. Develop samples (MF319 developer)
7. Rinse samples with distilled water
8. Dry samples with pressurized N₂ gas
9. Hard bake (90°C for 10 minutes)
10. Wet etching of chromium
11. Rinse samples with distilled water
12. Remove photoresist with acetone
13. Soak samples in IPA and rinse them with IPA
14. Dry samples with pressurized N₂ gas

After cleaning and drying the chromium-coated glass slides, BidTec spin-coater (Figure 3-4(a)) has been used to coat them with S1813 positive photoresist. A specific recipe was used for this type of photoresist for attaining the required thickness of 1.4 μm. The recipe used the speed of 3950 rpm at 30 s for spinning [62].

For the soft bake procedure, the photoresist-coated samples are placed in the oven with a temperature of 115°C for 7 minutes. This baking helps to dry the photoresist to some extent so that it will not stick to the mask during lithography. EVG620 aligner [63] is used for the top-side lithography process. Size and thickness of the mask, thickness of the photoresist layer, and thickness of the samples help to choose the suitable recipe for the lithography of the samples and modify it accordingly. These parameters are also needed to choose the appropriate fixtures; chuck, mask holder, and loading frame. The aligner and all its components are shown in Figure 3-4(b).

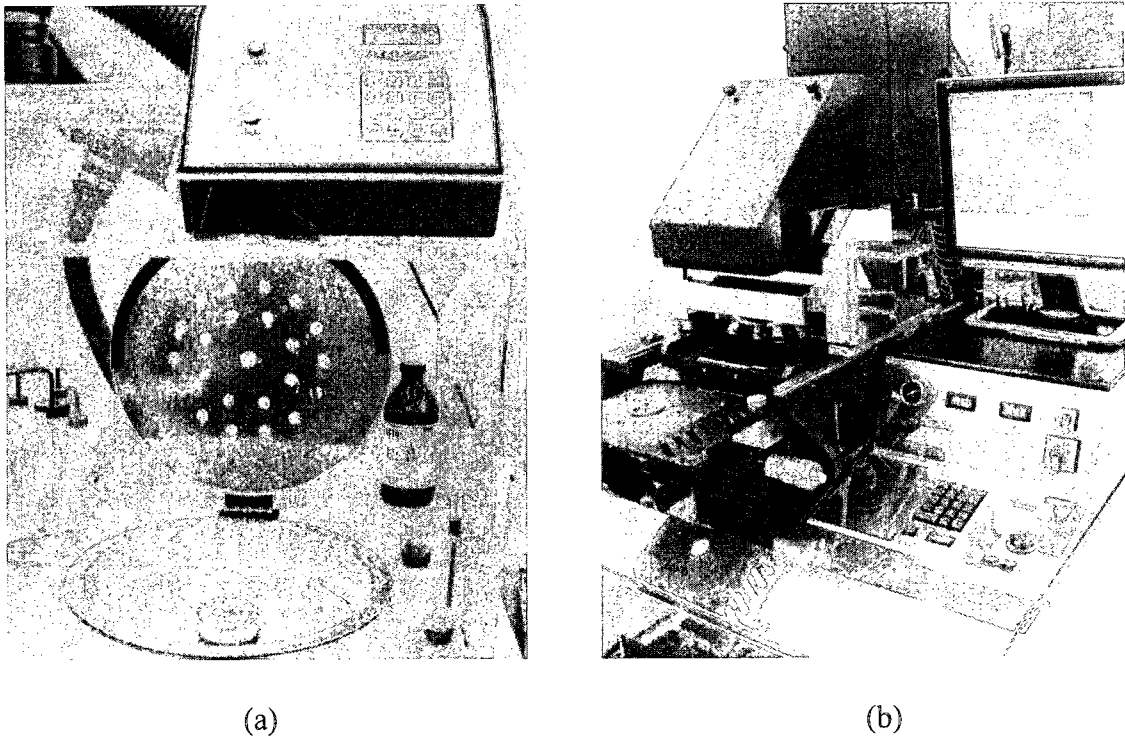


Figure 3-4 Photolithography equipments (a) BidTec spin-coater (b) EVG620

To develop the samples, MF319 developer is used. The samples have to be soaked in the developer for 45 seconds. Another 10 minutes in the temperature of 90°C is necessary for

the samples to make sure that the photoresist will not be removed during the etching process. This step is called hard bake. Then samples were soaked in Chromium etchant type 1020 with an etch rate of 40 angstroms per second at 40°C. The etching time is determined based on the chromium thickness. Checking out the samples under microscope ensured the complete removal of unwanted chromium.

After the chromium electrodes are prepared with a layer of photoresist on top, the only step remained is removing photoresist with acetone (regular cleaning). Although acetone is the best solvent to remove the photoresist, it may be needed to use it in higher temperatures about 45-50°C or even replace it with a stronger solvent such as Piranha solution (Strong cleaning solution). Piranha is a solution made of certain percentage of H₂SO₄ and H₂O₂. These cleaning methods are exactly used for cleaning the photomask. Next section describes the coating procedure of the insulating layer.

3.1.3. Insulating Layer

To provide a proper insulation against conductive fluids, the control electrodes are covered with an insulating layer. Pollack [11] studied several different materials as the insulator and found that Parylene C is the best choice for electrowetting applications. This polymer has high dielectric constant and dielectric strength, low static and dynamic coefficient of friction as well as good thermal, physical, and chemical stability. Parylene film is considered to be biocompatible and chemically inert. It also possesses a low intrinsic charge. Parylene C generates a conformal, pinhole-free and uniform insulating film on top of the electrodes. They have a wide range of crystallinity which is a function of deposition parameters and post deposition processing. Parylene films are chemically

resistive and also very difficult to be removed after deposition. Although they swell as the solvent absorbs into the bulk of the polymer, they never solve below their melting temperature.

Breakdown voltage of an insulator is the minimum applied voltage in which a portion of the insulating layer acts as an electrically conductive layer. Breakdown voltage of Parylene C depends on the thickness of the layer. Figure 3-5 presents a graph provided by SCS Company (Specialty Coating Systems TM, Indiana, USA) for the breakdown voltages. According to this graph, breakdown does not happen in our operating voltages. Thus, Parylene film is an excellent choice for the electrowetting experiments.

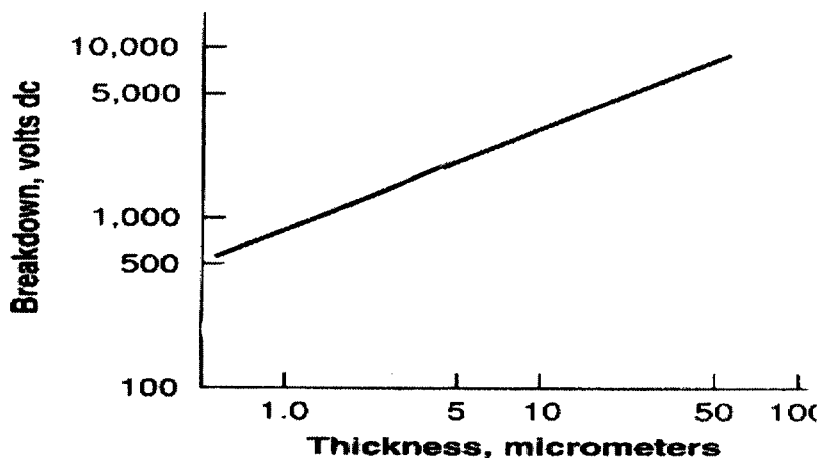


Figure 3-5 Voltage breakdown of Parylene C layer versus its thickness [from SCS company]

Parylenes are produced by a method of polymerization named chemical vapour deposition (CVD). In this method, a vapour of reactive monomer is produced and then introduced into the deposition chamber where it polymerize while adsorbing onto the surface [64]. This method of deposition has some advantages over the other polymerization methods. In other methods, an extra step such as heating is needed to

remove the solvent or initiate the polymerization. This extra step may cause problems such as non-uniform film thickness, pinholes, and non-conformality of the polymeric film, as well as remaining of solvent residues. In the CVD of Parylene there is no solvent used or produced and this process leads to a conformal and pinhole free films.

Gorham [65] devised the deposition method for Parylene films through the vacuum pyrolysis of di-para-xylylene (the dimer). Through this method, as shown in Figure 3-6, the dimer is cleaved into monomer units at temperatures above 550°C and pressures less than 1 Torr. Monomers are then adsorbed onto the surface at room temperature and polymerize.

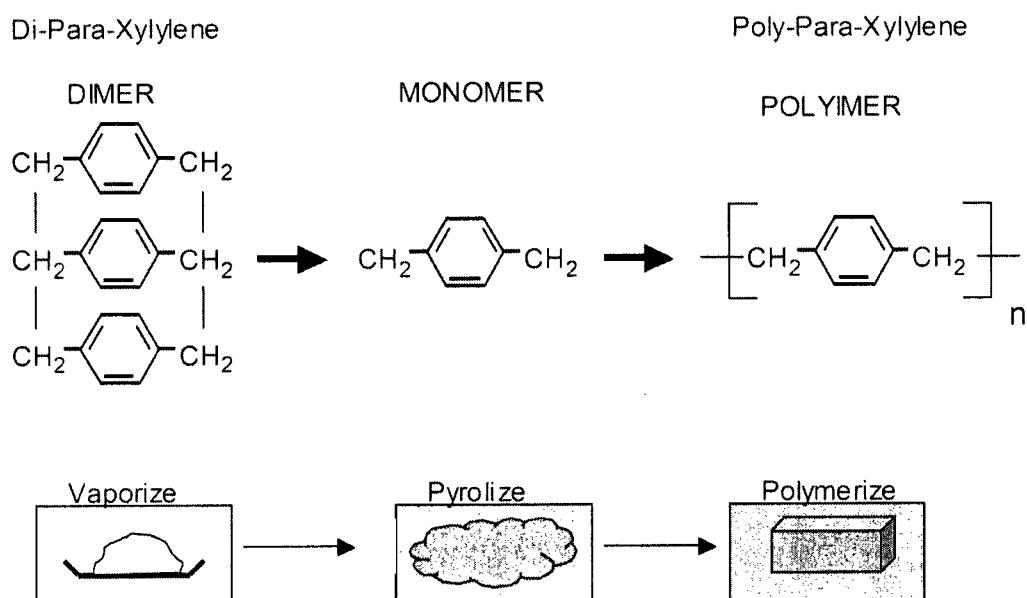


Figure 3-6 Parylene structure and composition [67]

The main pieces of a Parylene CVD system are the sublimation furnace, pyrolysis oven, the deposition chamber, and the vacuum pump. Some other necessary parts and

accessories include pressure measurement system, cold trap, and heating tapes to prevent specific parts of the system from polymer deposition. Figure 3-7 shows the Parylene C deposition system. Sublimation furnace is where the powder evaporates at 200°C and pyrolysis oven is where it changes to monomers at 700°C. The monomers then polymerize on the substrate surface at 20°C in the deposition chamber. The basic vacuum system for the coating machine consists of a mechanical pump and a cold trap. The mechanical pump can provide vacuum in the system into the low mtorr ranges. The cold trap is used to collect monomers that do not deposit in the deposition chamber. Temperature controlled substrate holder is made by sandwiching a thermoelectric cooler module between two thin polished copper plates. The bottom plate has cooling water lines in order to absorb the heat from the top surface. The wafer temperature is measured using a thermocouple positioned in a groove between the cover plate and the wafer.

It is well known that achieving a uniform Parylene film can be challenging due to the sensitivity of deposition to the operating conditions. This unfavourable feature is most likely because of the pressure variations within the deposition chamber, or temperature variation taking place in ovens and substrate surface. The measurement methods can produce significant errors. Devices like a capacitance monometer measure the pressure directly while sensors like a thermal conductivity gauge measure the pressure indirectly, by measuring the thermal properties of the gas. The measurement errors usually happen in the indirect measurement gauges. At low pressures the deposition rate will drop to zero, at high pressures the films can get milky in appearance and have very rough surfaces with globular structures. Sample preparation (cleaning) and dimer purity are two other crucial factors in the quality of the Parylene film. Some of the useful equations for

calculating Parylene deposition parameters such as flow rate, residence time, and deposition rate are given in Appendix A.

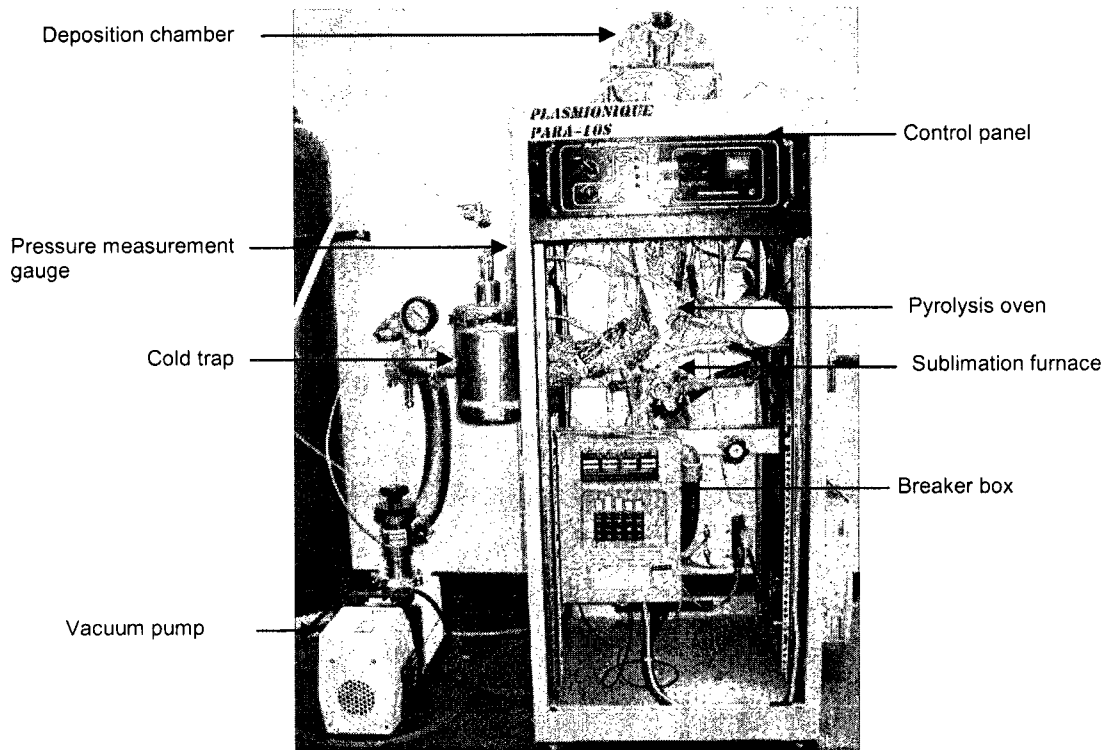


Figure 3-7 Parylene coating machine, PARA-10S

The thickness measurement has been done using AFM. For this purpose, a scratch was made on the layer and the measurements have been performed on several different spots of the scratch and the results confirmed a uniform thickness of 800 nm of Parylene C. Figure 3-8 shows one of the results. The vertical distance between two red triangles on the graph is the representative of the thickness. As it is written in this figure, RMS roughness of the coating is 12 nm. The average measured roughness is 10 nm which verifies the high quality of the layer.

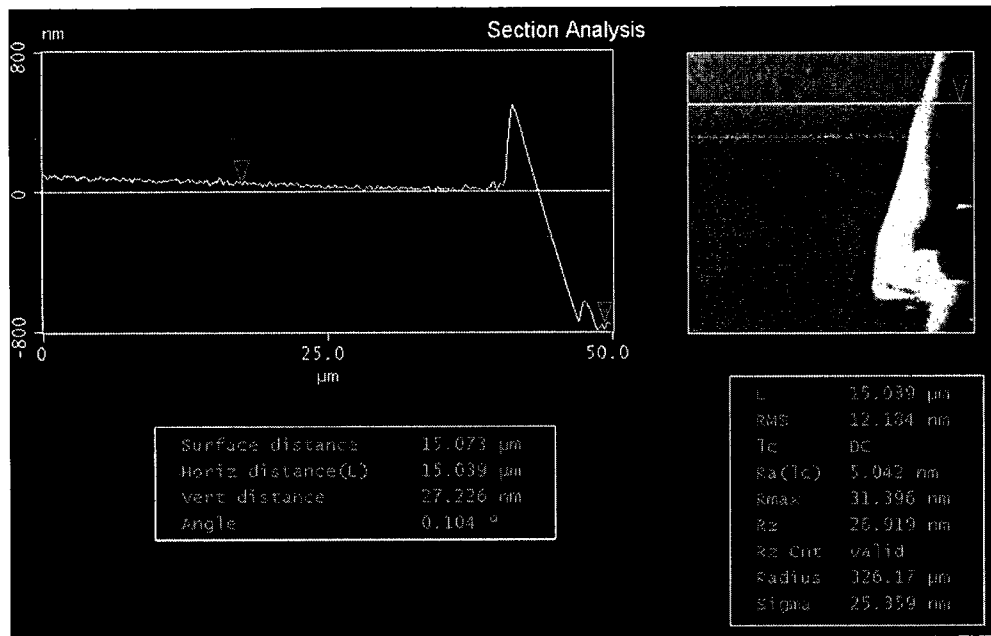


Figure 3-8 Thickness measurement of Parylene layer using AFM

3.1.4. Hydrophobic Layer

Although Parylene C is hydrophobic, it is still required to create a hydrophobic surface with the contact angle about 109° to provide a larger contact angle range from hydrophobic to hydrophilic. A 1% M solution of Teflon AF 1600 has been chosen for this purpose. Teflon shows very good chemical resistance, low surface energy, and high temperature stability. However, it could not be chosen as the insulating layer because of its rather low dielectric constant. BidTec spin coater is used to coat Teflon AF (1% M solution) on top of the insulator layer. The required thickness would be 50 nm and this has been gained by using a rotation speed of 3000rpm, and a time period of 20 seconds as spin parameters.

The thickness of Teflon layer plays a pivotal role in the experiments. Dielectric constant of Teflon is not as large as that of Parylene C; however, thick layer of Teflon adds capacitance to the circuit, on the other hand, a thin Teflon layer can be removed easily during experiments. A surface profiler (Veeco Dektak) was used to characterize the Teflon layer. As the surface profiler operates based on material refractive index, it is not able to detect transparent layers. Therefore, the Teflon layer was coated with a 90 nm layer of gold after scratching for measuring its thickness. Gold layer was deposited using a gold sputtering machine. Figure 3-9 shows the distance between two points on the Teflon layer which represents the thickness. It also gives a 10 nm average roughness for the coating for this specific specimen. The average roughness achieved by measuring the thickness in different samples is 5 nm which is sufficiently good for our application.

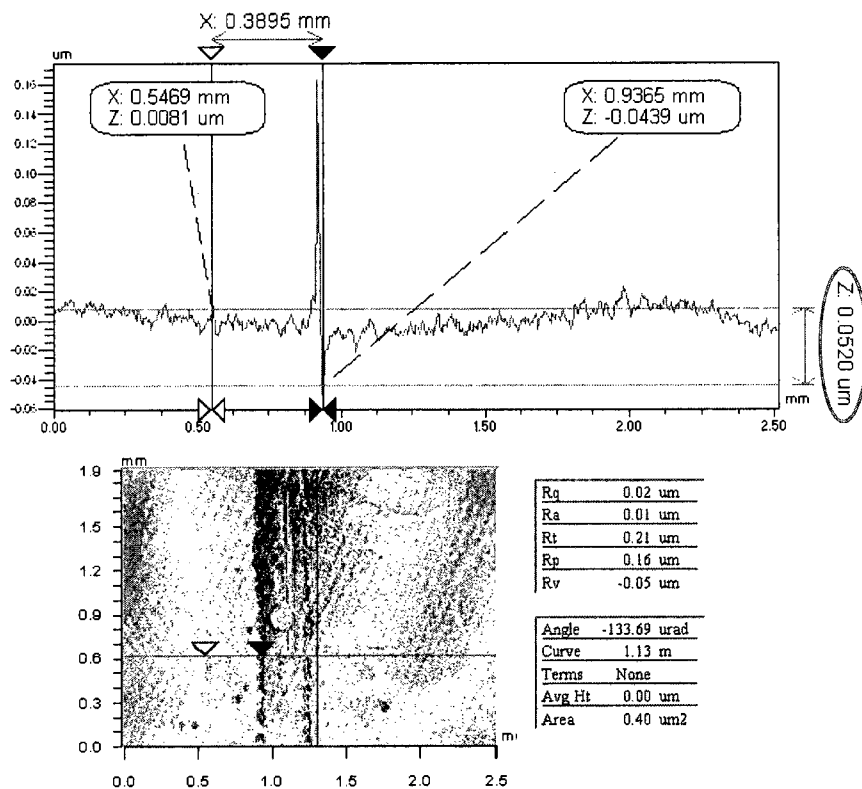


Figure 3-9 Thickness measurement of Teflon layer using surface profiler

3.2. EXPERIMENTAL SETUP

Besides fabrication of the samples, a setup is also needed to perform the experiments. This section introduces the apparatus used in the experiments as well as the electrical board which has been designed to control the droplet movement on the array. It is needed to use a positioner to adjust the gap between two parallel plates, i.e. the control electrodes and the ground electrode. On the other hand, the rig is designed in a way that it provides space for cameras of top and side views.

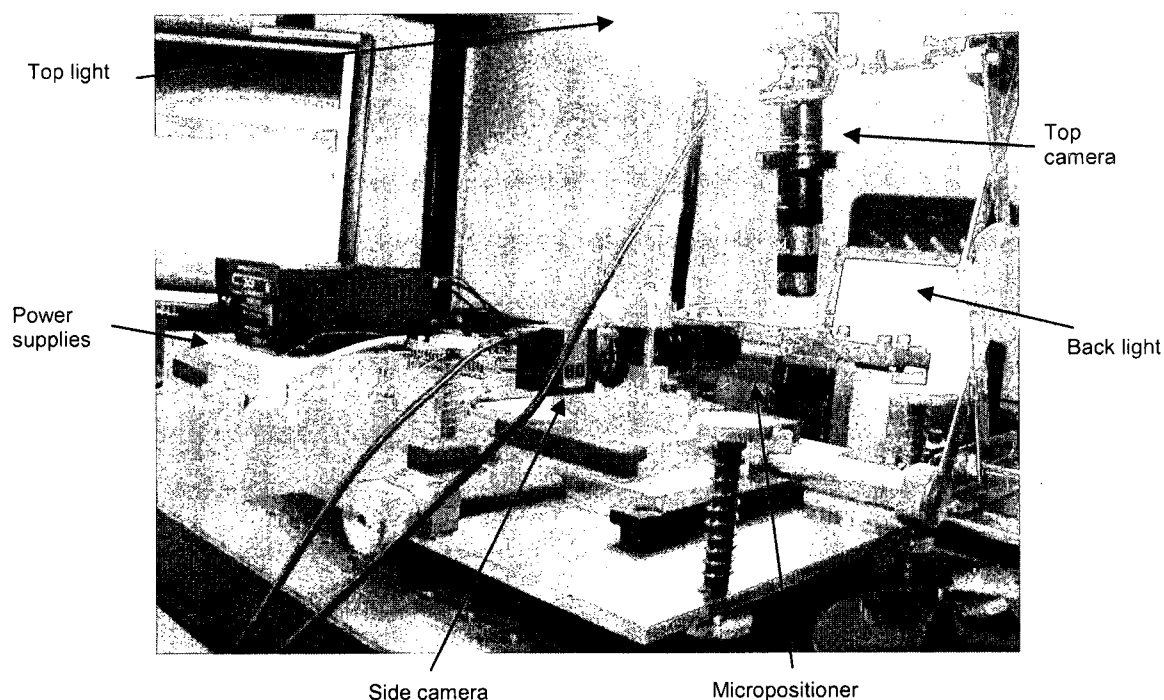


Figure 3-10 Experimental setup

The experiments have been conducted by the apparatus in which a droplet of 0.1 M KCl solution is sandwiched between electrode coated plates. The gap spacing between the two plates was established by moving the bottom plate up or down via a micropositioner with

an accuracy of 5 μm . The droplet is dispensed by a digital syringe with an accuracy of 0.02 μL . The cameras used in the experiments are from EO series of Edmunds Optics and can capture up to 25 fps with a resolution of 2560×1920 pixels. Figure 3-10 shows the setup which was used in the experiments. Using this setup, the droplet movements from both top and side views were recorded simultaneously. The applied voltage in the experiments was limited to 65V DC. Although there was no dependency on polarity detected in the experiments, the tests were done with the positive polarity with respect to the ground electrode. In order to be able to move the droplet on an array of adjacent electrodes, a controller has been designed which can switch the electrodes in a sequential mode with a variable frequency.

3.3. GEOMETRY

The droplet and electrode geometries chosen for experiments and simulations are given in Figure 3-11. The modeled crescent electrode has a length of 1500 μm from the beginning to the end point with a width of 1500 μm as well. The radius of the crescent electrode has been chosen to be 950 μm . Being able to fairly compare two different shapes of electrodes, an array of flat electrodes with the same length of crescent electrode has been used. This array results in the same equivalent length of crescent electrode and is a sufficient length for the droplet to reach to the steady state velocity. Moreover, it is important to mention that the length of any single electrode should be at most equal to the droplet diameter in order to avoid the backward.

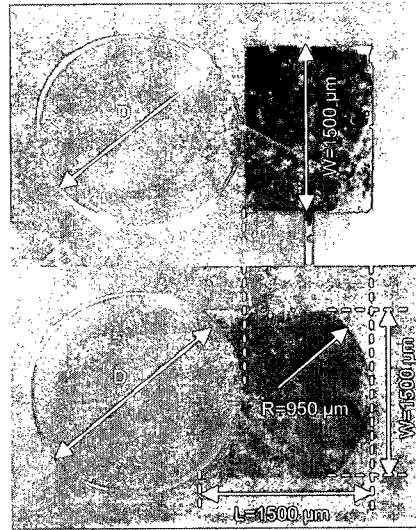


Figure 3-11 Geometry of flat and crescent electrodes

4. RESULTS AND DISCUSSIONS

This chapter presents both numerical and experimental results in order to explain the effect of electrode shape on the droplet manipulation via electrowetting. First, the results obtained from the new modified code are presented and compared by the previous model. Second, the use of new electrode shape is justified by comparing the droplet deformation and velocity during its movement.

4.1. MODEL IMPROVEMENT

The simulations are performed by a 3D FORTRAN code which is based on the VOF technique (explained in chapter 2). In this work, the dynamic contact angle model has been appended to the code. Moreover, a new method has been applied to compute the

electric field in the domain. The results obtained by the new model are studied by comparing the droplet velocity, the contact angles, and the electric field distribution.

Figure 4-1 shows a stationary droplet placed on a Teflon surface. Based on the experiments performed, the droplet static contact angle on the Teflon coated surface is $109\pm 3^\circ$. This contact angle is fed into the code as the initial contact angle. In the static model, by advancing the droplet on the electrode with an applied voltage of 55 V, the contact angle at the leading edge decreases from 109° to 67° while the contact angle at the trailing edge stays constant at 109° . Meanwhile, using the dynamic model results in a range of contact angles for the droplet leading and trailing edges. The dynamic contact angle at the leading edge changes between 67° and 75° while the contact angle at the trailing edge varies between 101° and 109° .

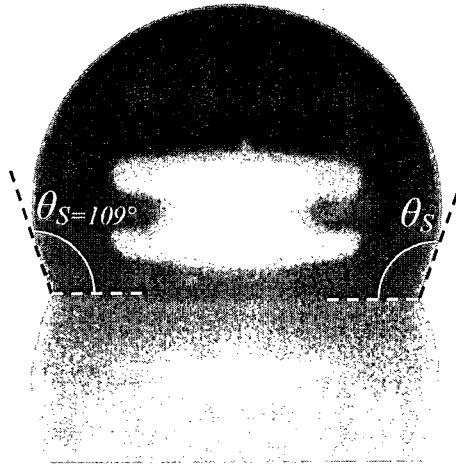


Figure 4-1 Static contact angle of a droplet sitting on a Teflon surface

Figure 4-2 compares the contact angles of the static model with those of the dynamic model. Trailing edge of the droplet shows a contact angle of 109° which is the static contact angle of the droplet on Teflon surface in the absence of the electrical actuation. When the droplet leading edge is affected by the electric potential as seen in the same figure, this contact angle changes to 67° . Depending on the contact line velocity, the dynamic model changes the leading and trailing contact angles to a range of 67° – 75° and 101° – 109° , respectively. Therefore, the leading edge contact angle is increased by 8° while the trailing edge contact angle is decreased by 8° at the maximum contact line velocity. Thus, the change in contact angle results in a decrease in the net force acting on the droplet which leads to different droplet behaviour predicted by static and dynamic models.

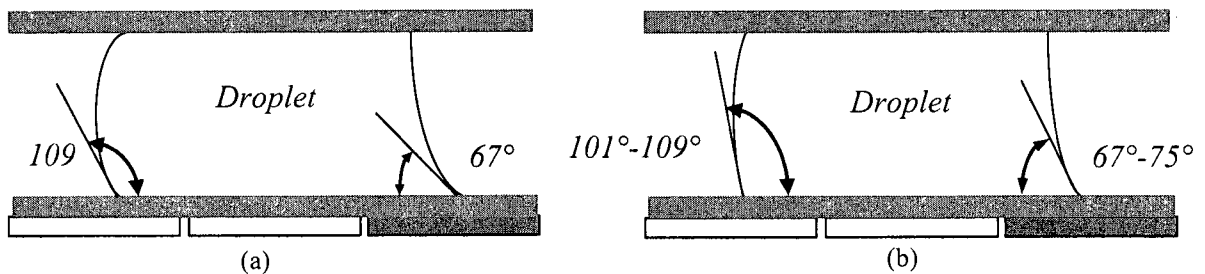


Figure 4-2 Schematic view of droplet contact angle on the Teflon surface actuated at 55 V (a) Static (b) Dynamic

Considering the molecular-kinetic model, the contact line motion is related to the adsorption of molecules on the surface [47]. These interactions act as the main barrier to the motion of the wetting line and make the molecules immobilized. In this dynamic model, numerical simulations present a lower velocity for droplet in comparison with the

static model. Figure 4-3 demonstrates the droplet velocity computed by the static and dynamic contact angle approaches. The data belong to a droplet with $1900\ \mu\text{m}$ actuated by flat electrodes at $55\ \text{V}$. Dynamic model predicts slower movement for droplet due to molecular level adsorption and dissipation. However, both dynamic and static models show similar results at the onset of actuation due to the small contact line velocity at the beginning of droplet motion.

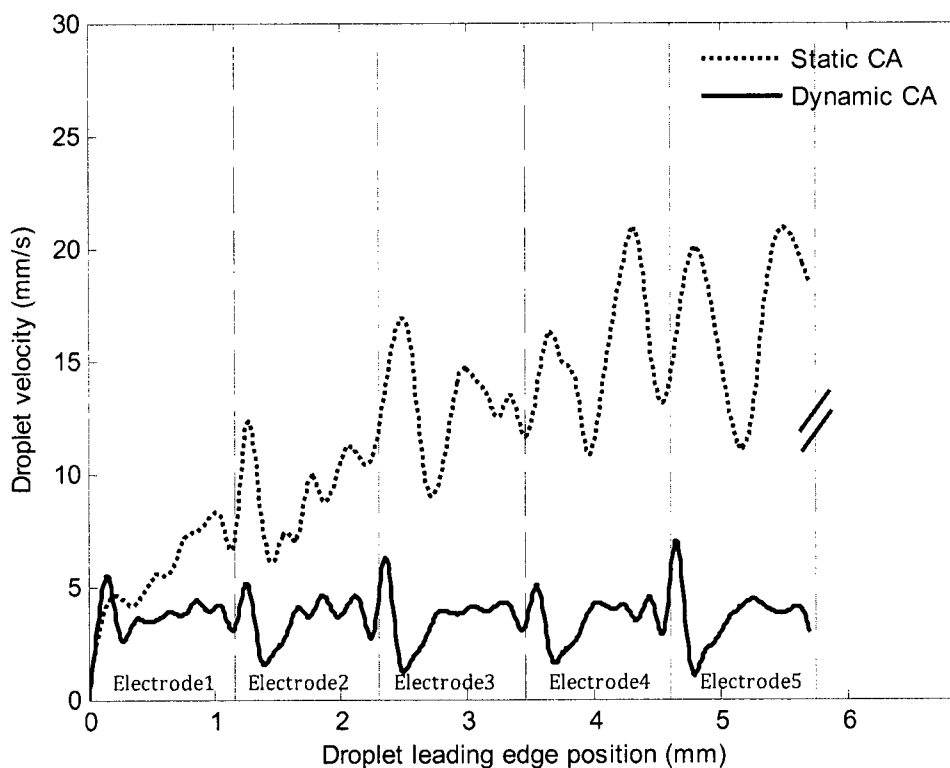


Figure 4-3 Droplet velocity on an array of flat electrodes for static and dynamic models

The other modification applied to the code is the new implementation of electric field at the tri-phase line. Figure 4-4 demonstrates the voltage distribution at the leading edge of

the droplet actuated at 55 V using two different methods. Using the new algorithm results in actuating the droplet on a larger portion of the contact line by precisely estimating the voltage in the interfacial cells close to the electrode corners. In addition, a smooth distribution of voltage is achieved on the droplet interface.

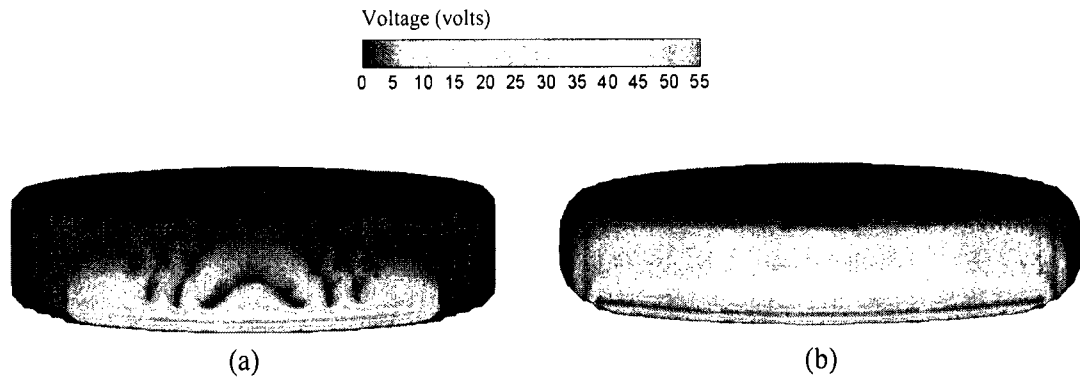


Figure 4-4 Interfacial voltage distribution (a) using average voltage (b) using new voltage implementation

The distribution of equipotential surfaces for an actuation voltage of 55 V is illustrated in Figure 4-5. In this figure, a 3D view of the voltage distribution is shown for half of the domain for a droplet with a diameter of 1900 μm in the middle of a crescent array. The implementation of the new algorithm for voltage calculation results in a smooth dissipation of electrical energy from the powered electrode to the grounded droplet. According to the studies by Zeng and Korsmeyer [30], the forces exerted on the liquid-gas interface are negligible when the ratio of the insulator thickness to channel gap is small. Thus, the only important force is the one which acts on the droplet tri-phase line.

This force becomes greater when the contact line approaches the electrode and it leads to decrease the contact angle at the tri-phase line and finally results in moving the droplet.

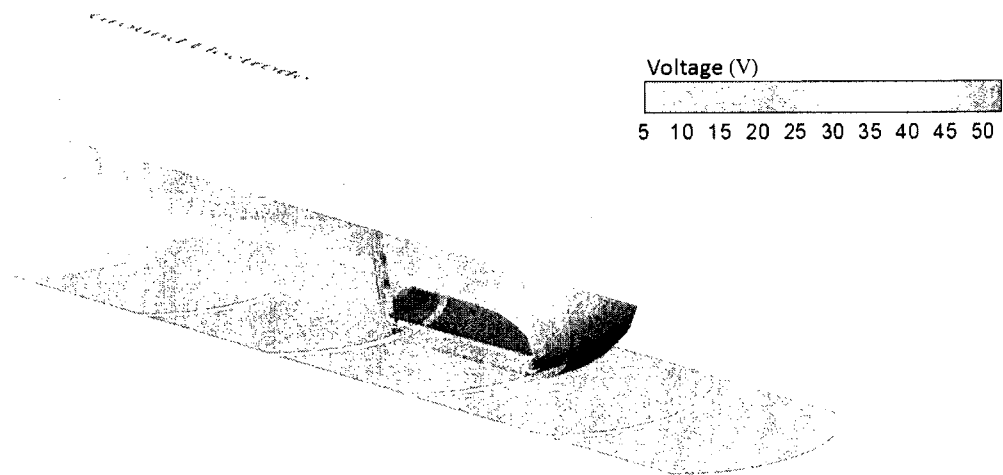


Figure 4-5 A 3D schematic of electric field applied on the droplet in a channel

The implementation of the new algorithm in voltage calculation subroutine has significant effects on the droplet velocity in the microchannel. Figure 4-6 shows the droplet velocity on an array of 6 flat electrodes sequentially actuated at 55 V. This graph compares the droplet velocity obtained by the corrected voltage model and the previous model. As shown and explained in Figure 2-4 , the voltage applied on the droplet interface is overestimated at the onset of actuation using the old model. By solving the Laplace equation on substrate surface and retaining the voltages at the interfacial cells using the new model, the overestimation associated with the old model has been resolved. Therefore, the droplet velocity at the beginning of the first electrode decreases.

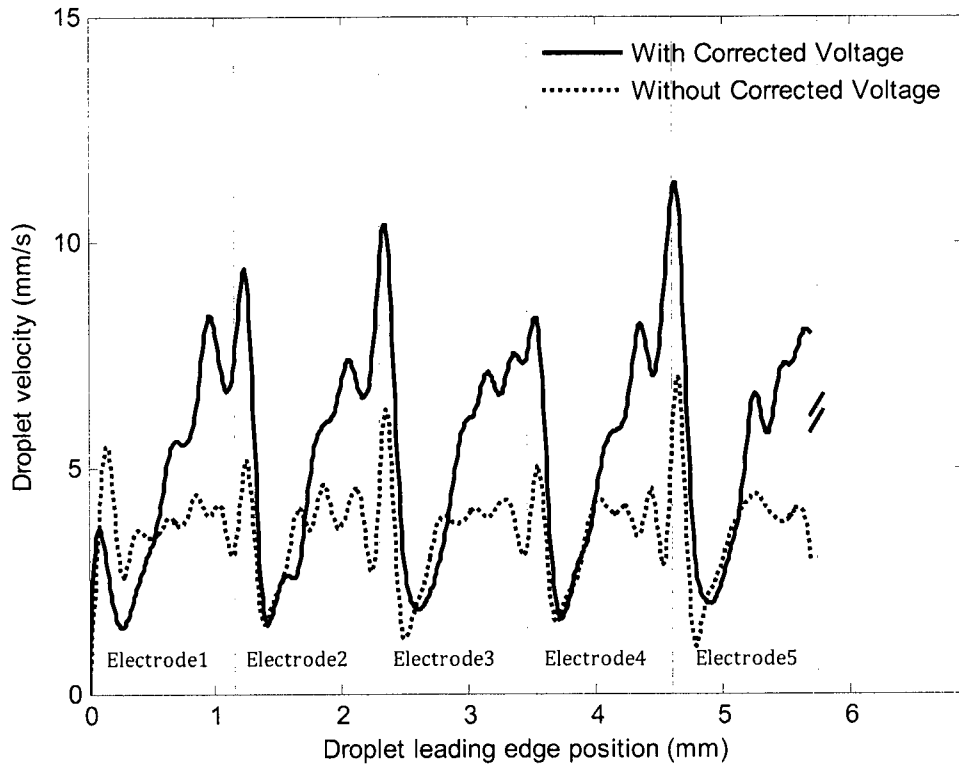


Figure 4-6 Droplet velocity on an array of flat electrodes with and without voltage correction

The velocity of droplet leading edge reaches to a maximum when the leading edge is at the end of each fired electrode. The force resulted from the contact angle change, which is in favor of the movement, causes the acceleration of the droplet until the electrode end. The velocity drops suddenly when the droplet advances on the next fired electrode. During the droplet transition from one electrode to another, the affected contact line decreases from maximum portion Figure 4-7(a) to its minimum one Figure 4-7(b) on a flat electrode. This is found to be the reason of sudden reduction in velocity. When the velocity is plotted based on the leading edge position, the maximums are exactly located at each electrode end. In this work, this maximum point is shifted forward because the

velocities shown here are based on the average velocity of droplet leading and trailing edge. The droplet center reaches to the maximum velocity later than the droplet leading edge.

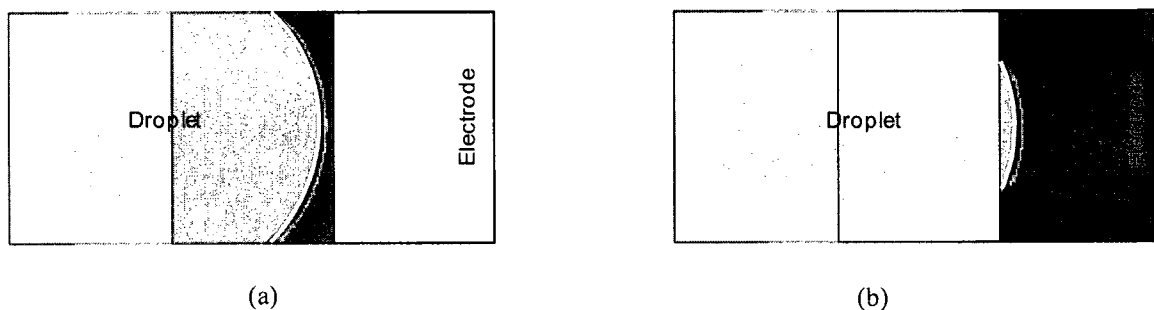


Figure 4-7 Actuated droplet contact line on flat electrode (a) at the electrode end (b) at the beginning of the electrode

The maximum velocities at the electrode ends are increased up to 80% using the new model. In the new method, all the interfacial cells at the droplet leading edge, even the cells away from the electrode, experience an amount of voltage based on the Laplace calculations Figure 2-5. These cells have been considered with zero voltage in the previous method Figure 2-4. This can be the reason for having higher velocities at transition points of electrodes.

All the velocity graphs follow a similar scheme of averaging described below. Figure 4-8 shows the droplet velocity on the first electrode based on leading edge, trailing edge, or mid-point. At the beginning of motion, droplet leading edge gains a nonzero velocity while the trailing edge is still at rest. Afterward, the droplet trailing edge starts to move. From the beginning of the leading edge movement until the first advancement of the

trailing edge, the leading edge velocity increases. When the trailing edge starts to move, the leading edge velocity suddenly decreases from its maximum value. As illustrated in Figure 4-8, the maximum velocity reduces when plotted based on the droplet mid-point velocity. To better estimate the droplet the average velocity of leading and trailing edges are plotted. This velocity is based on the displacement of the droplet center which is considered in the middle of trailing and leading edge. Due to the large number of velocity

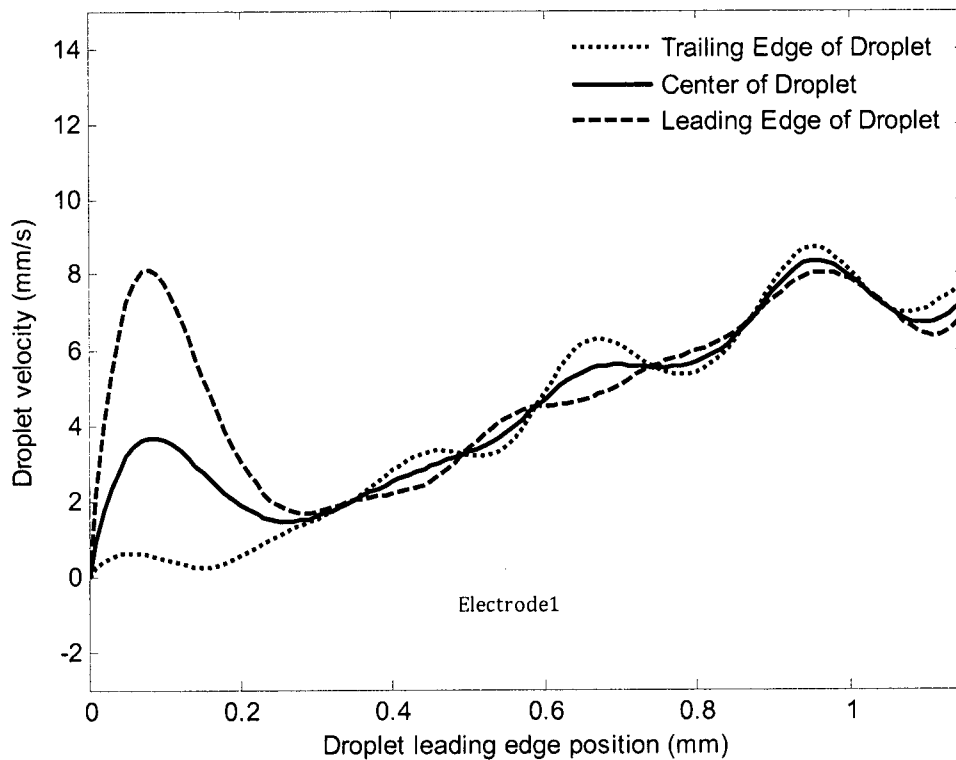


Figure 4-8 Droplet velocity based on trailing edge, mid-point, and leading edge

data being computed numerically, a bin-averaging scheme has been applied to the raw data. A Matlab program was written to sort and average the data all over the domain. In

this program, all the velocity data are discretized based on the arbitrary increments in the x direction. The average of all velocity data in each incremental step is considered as the velocity in that increment and the x position of the middle of the increment is where that averaged velocity happens. Then, cubic spline interpretation is utilized to fit a curve to the data. This method is applied to produce all the numerical velocity profiles presented in this work.

As explained in chapter 2, the effects of dynamic wetting and electric field are superimposed in the code. The final model shows good agreement with the experimental data. Figure 4-9 clarifies the effect of dynamic and electric field modifications on the droplet velocity for a droplet on an array of 6 flat electrodes sequentially actuated at 55 V. Having applied the new model, the droplet behavior during transport from one electrode to another is accurately modeled. The velocity reaches to its maximum when the droplet leading edge is at the end of each electrode. Therefore, the velocity profile on a series of electrodes looks like a periodical ramp function. The decrease in velocity applied by the dynamic model and the increase caused by the voltage modification leads to an overall reduced velocity for the droplet. The velocities obtained from dynamic model are $\frac{1}{7}$ of the velocities calculated by the static model. On the other hand, the new voltage implementation calculates the velocities twice the old velocities. However, the superposition of these two effects results in the reduction of velocities by $\frac{1}{4}$ which is shown in Figure 4-9.

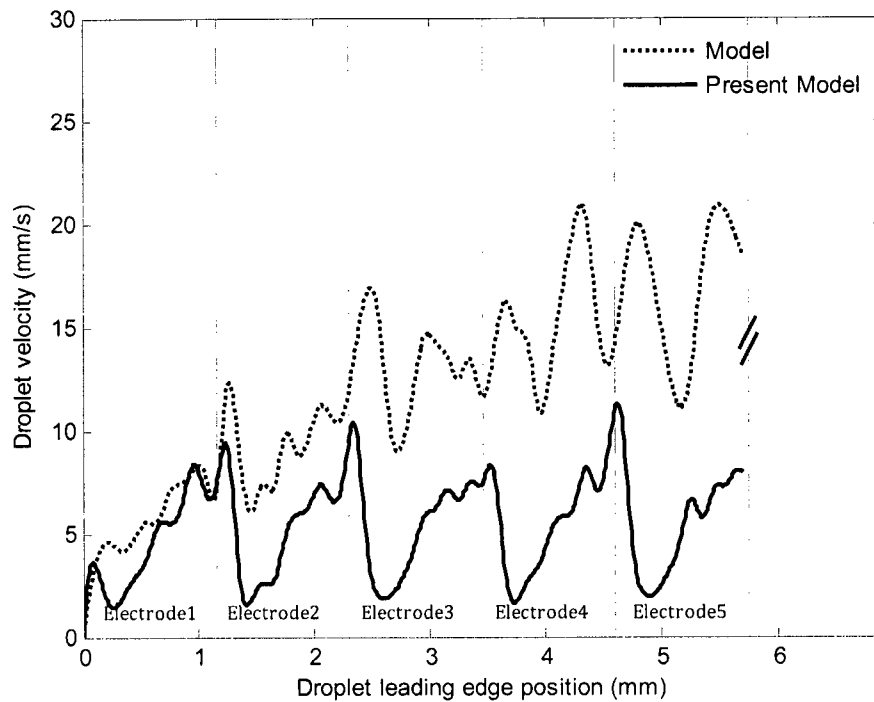


Figure 4-9 Droplet velocity on an array of flat electrodes using previous and modified models

4.2. DROPLET MORPHOLOGY

The electrode shape has a determining effect on the onset of actuation as well as droplet transition from one electrode to another. Depending on the actuated length of contact line, droplet deforms and moves differently, especially at the beginning of each electrode. Therefore, the droplet morphology and the contact angle distribution are the factors which can be used to examine the advantages of using crescent electrode compared to a flat electrode.

Crescent electrode can preserve the droplet shape to a very good extent at the onset of actuation and during the movement. This novel electrode shape also prevents the

excessive droplet stretching which can result in undesirable splitting. Figure 4-10 shows different steps of droplet advancement on both flat and crescent electrodes and provides a one-to-one comparison between experimental and numerical data. In these experiments, a voltage of 55 V has been applied to the electrodes to manipulate the droplet with a diameter of 1900 μm . Superior performance of crescent electrode can be deduced by comparing the time required for the droplet to reach to the end of electrode. This figure insists on the perfect agreement exists between the experimental and numerical results, as well as the less deformed droplet using crescent electrode.

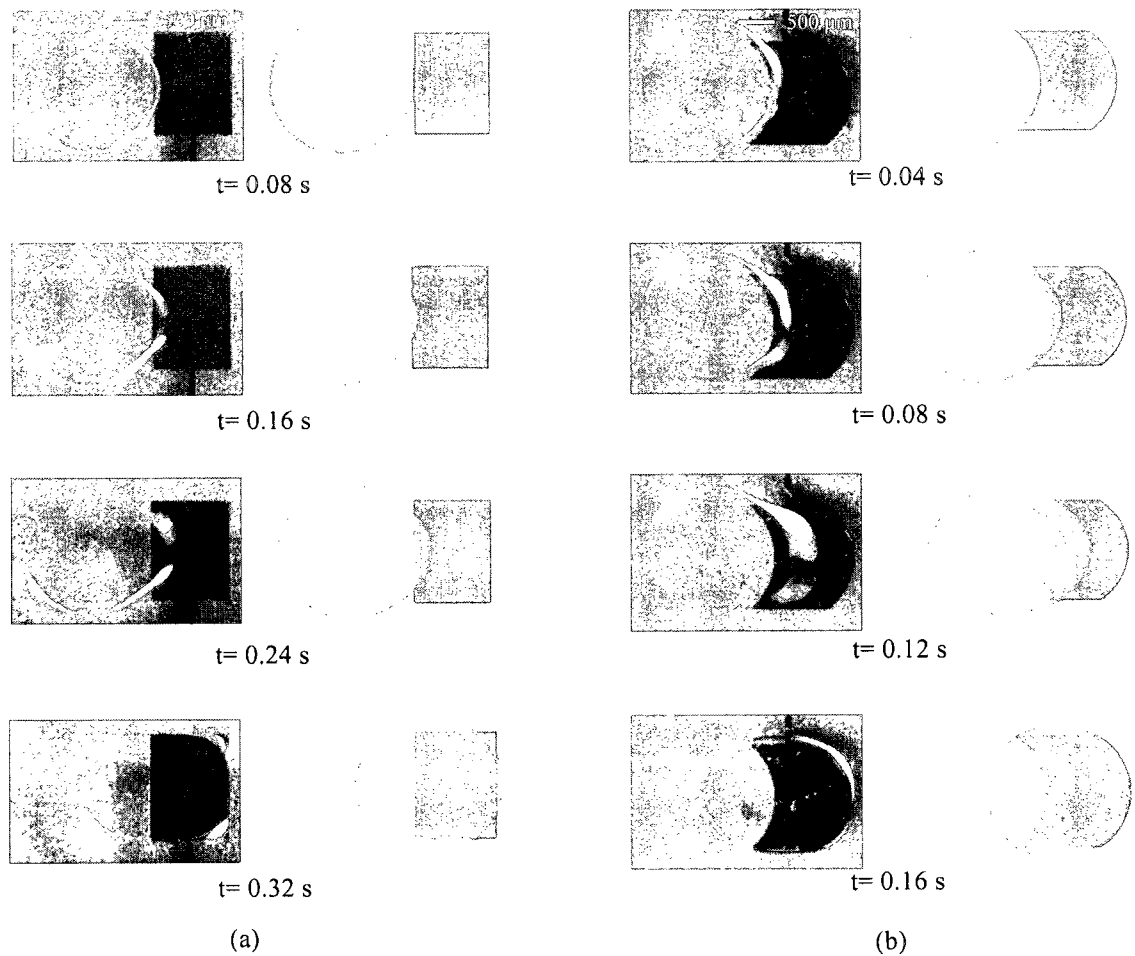


Figure 4-10 Experimental and numerical results for droplet advancement on a single electrode (a) flat (b) crescent

The deformation and actuation of droplet can be well explained by examining the contact angle distribution. The droplet is primarily at rest and when there is no actuation force, a uniform contact angle of 109° exists. Figure 4-11 (a, b) show the contact angle distribution for a droplet advancing on the flat and crescent electrodes, respectively. A

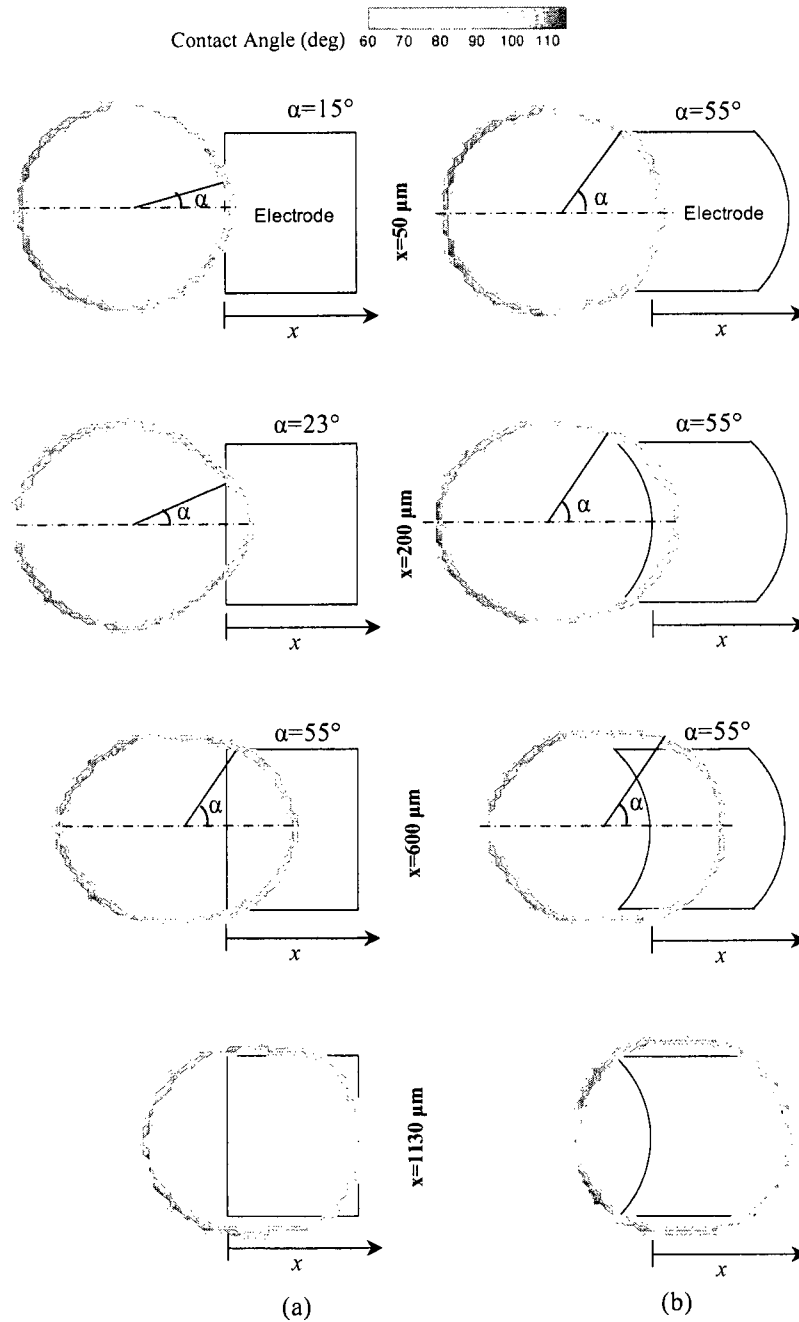


Figure 4-11 Contact angle distribution of a droplet on a single electrode (a) flat (b) crescent

voltage of 55 V has been applied to the electrodes. At $x=50\ \mu\text{m}$, a portion of the droplet with a polar angle, α , of 15° experiences a contact angle decrease to 67° on the flat electrode while using the crescent shape this affected portion of the contact line is 55° . The actuated contact line on the flat electrode increases to 23° at $x=200\ \mu\text{m}$ and finally 55° at $x=600\ \mu\text{m}$. However, the droplet on the crescent electrode is actuated with a polar angle of 55° during the entire actuation process. The leading edge of the flat electrode should move $600\ \mu\text{m}$ (almost half of the electrode length) to reach to α of 55° . The droplet on the crescent electrode has the higher velocity because its contact line is fully actuated from beginning of the motion. Although the droplet on the flat electrode is ultimately actuated with the same affected area of crescent electrode, its energy is dissipated to deform and stretch instead of moving forward. The adapted shape of electrode can create a uniform electric force on the droplet periphery. This electric force leads to a homogenous stretching of the droplet contact line in a radial direction oriented outward from the droplet and consequently, it prevents the droplet from large deformation.

4.3. DROPLET VELOCITY

Providing faster movement and easier actuation for the droplets is the goal of using crescent electrode. This part of results compares the velocities obtained using flat and crescent electrodes. Numerical results along with the experimental ones are presented to prove the excellent performance of the crescent electrode.

4.3.1. Single Electrode

First, the numerical simulations and validating experiments are presented for a droplet actuated on a single electrode. Figure 4-12 shows the velocity profile of a droplet with different diameters on the flat and crescent electrodes charged by 55 V. This figure shows the agreement between the numerical and experimental results and also confirms the higher velocity of the droplet moved using the crescent electrode. According to these graphs, the maximum velocity occurs when the droplet leading edge is just before the end of electrode. At the onset of actuation, the velocities obtained by using the crescent electrode are up to 4 times of those on the flat electrode.

To show the range of droplet sizes which can be actuated by the, droplet maximum velocity is plotted in Figure 4-13. This figure can also be served to compare the sensitivity of the crescent and flat electrodes to the droplet size. Different droplet sizes are chosen to cover the droplet curvatures either smaller or larger than the crescent electrode curvature. To find the maximum velocity, a quadratic curve is fitted to each velocity profile. The maximum velocity happens at $D/W=1.067$ for both electrode shapes which is associated with $D=1600\ \mu\text{m}$ in this case. The crescent electrode is capable of moving the droplets with almost double the droplet velocity on a flat electrode. This is a magnificent characteristic of the crescent electrode which is due to the creation of such uniform electric field on the droplet interface.

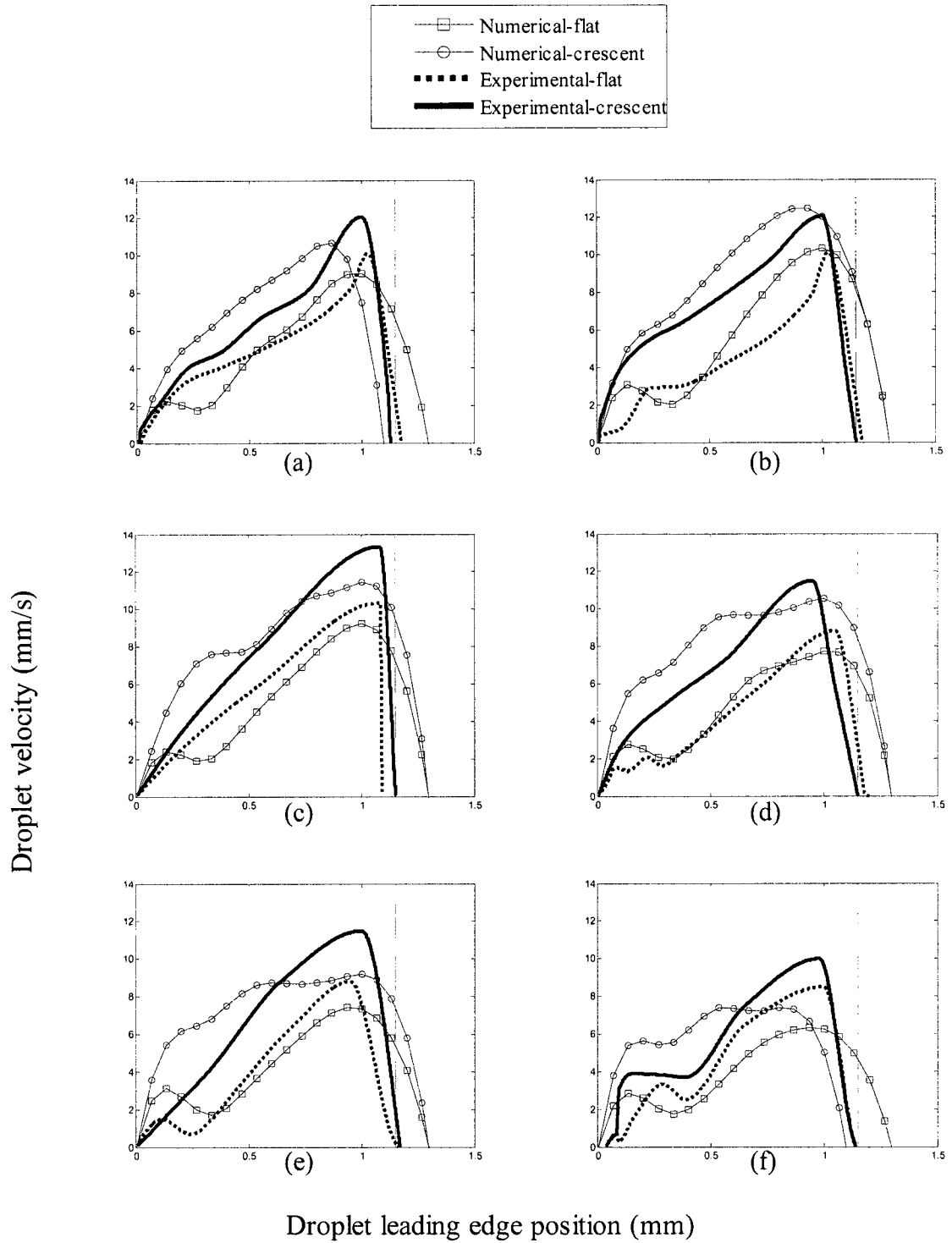


Figure 4-12 Experimental and numerical results of droplet velocity on a single electrode for various droplet diameters (a) $D=1500\ \mu\text{m}$ (b) $D=1600\ \mu\text{m}$ (c) $D=1700\ \mu\text{m}$ (d) $D=1800\ \mu\text{m}$ (e) $D=1900\ \mu\text{m}$ (f) $D=2000\ \mu\text{m}$

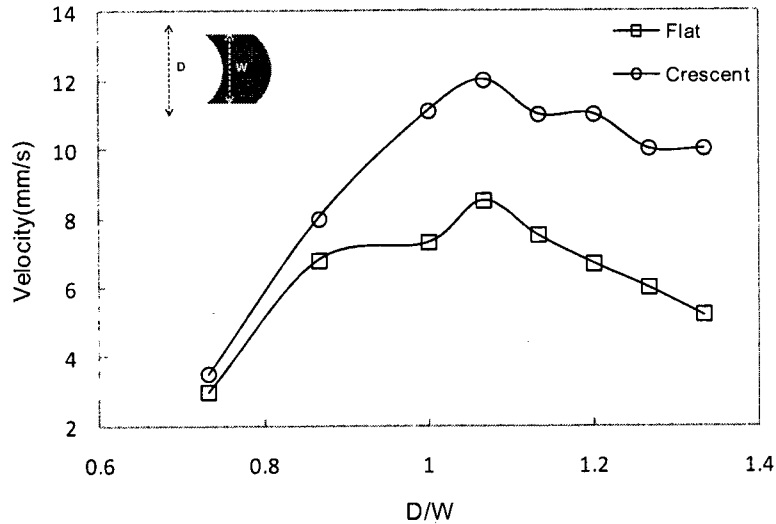


Figure 4-13 Droplet maximum velocity on a single electrode for various droplet sizes

Surfing more into the superior performance of crescent shape, some specific cases have been experimentally observed to certify the easier and faster actuation provided by the crescent electrode beside its higher velocity. The novel crescent shape is capable of moving droplets even when the droplet is not placed on the electrode. Figure 4-14 shows the incomplete movement of droplet with a diameter of 2000 μm on a single flat electrode at 55 V while the crescent electrode is able to move the same size droplet toward the electrode end. In this experiment, droplet leading edge is touching the front edge of the electrode at the beginning of experiment for both cases. Figure 4-15 (a) shows another incomplete movement of a droplet with a diameter of 1900 μm on a flat electrode charged at 55 V. Interestingly, the crescent electrode was capable of thoroughly move the same size droplet with the same applied voltage even with a 20 μm initial distance between the droplet and the electrode (Figure 4-15(b)). It was also observed a droplet actuation with the crescent electrode when its leading edge is 40 μm away from electrode. These

experiments prove the outstanding performance of the crescent electrode in easier actuation of droplet.

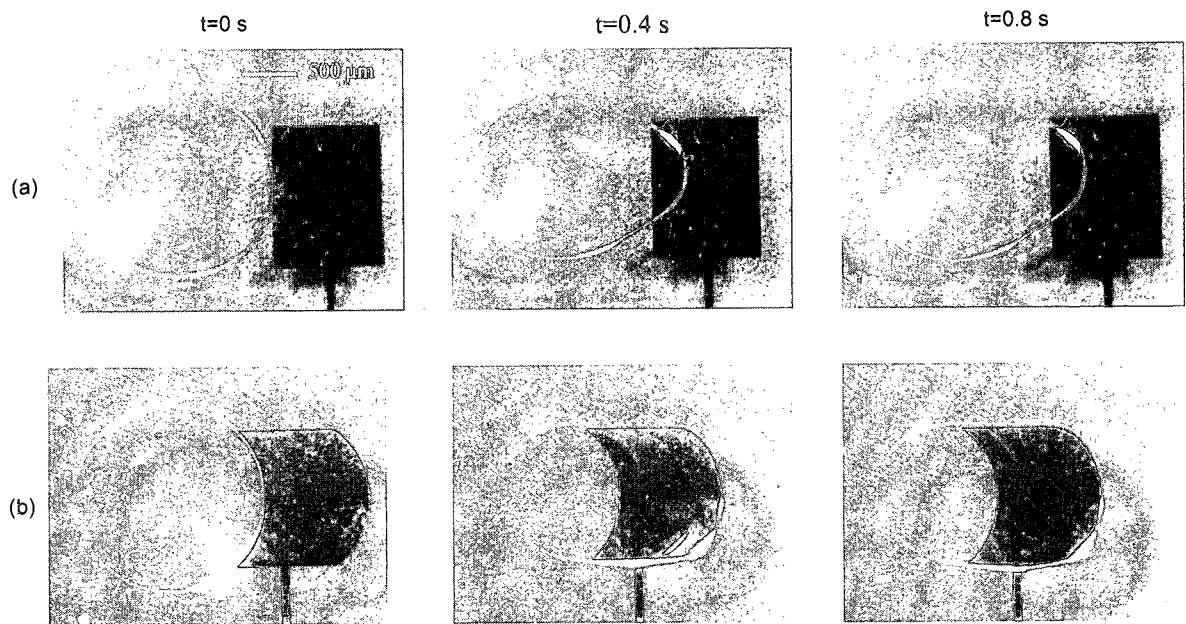


Figure 4-14 Actuation at 55 V for a droplet with the diameter of 2000 μm touching the electrode in a channel with the height of 200 μm (a) flat (b) crescent

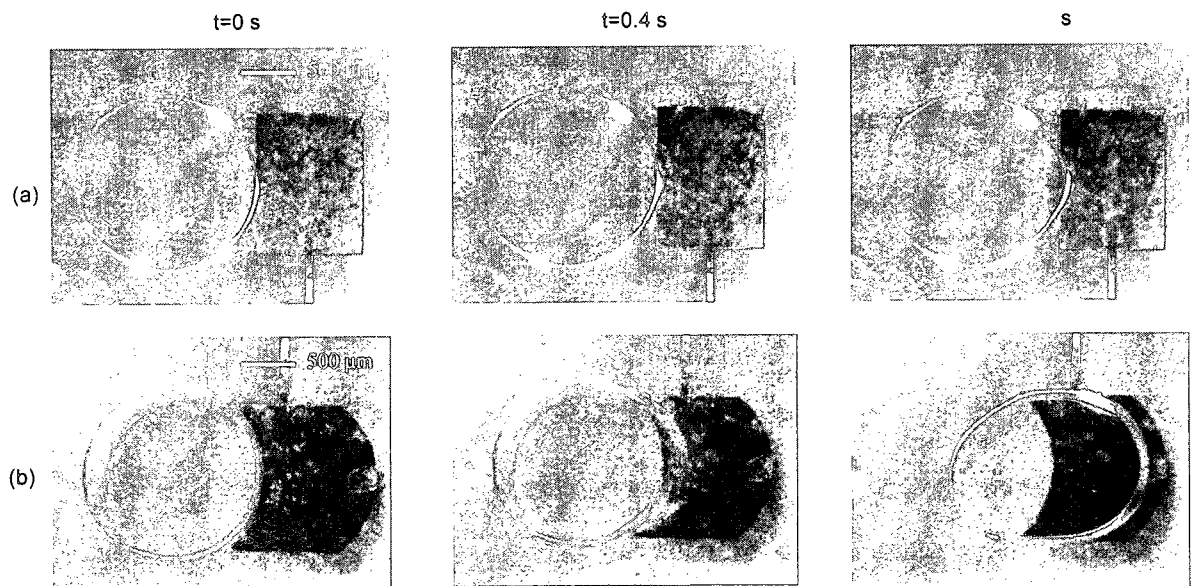


Figure 4-15 Actuation at 55 V for a droplet with the diameter of 1900 μm in a channel with the height of 300 μm (a) touching flat electrode (b) 20 μm far from crescent electrode

4.3.2. Electrode Array

Having discussed the onset of actuation for the droplets on single electrodes, the droplet velocity on electrode arrays is studied. The droplet location in three different instants of its movement on an array of electrodes is another way to show the higher droplet velocity using the crescent shape electrodes. Figure 4-16 illustrates that the droplet moves all the way to the end of the crescent electrode array in 0.7 seconds, while at the same time it only reaches to the middle of the flat electrode array.

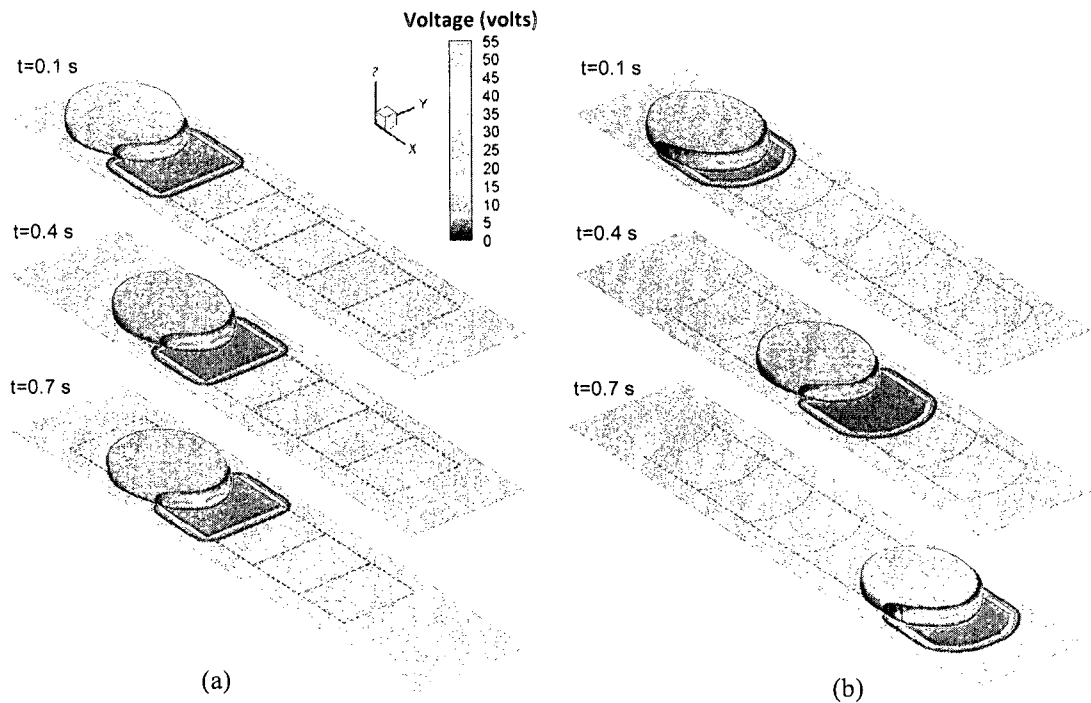


Figure 4-16 Numerical results of droplet movement on array of electrodes (a) flat (b) crescent

Further details of droplet motion and oscillation on electrode arrays are described in Figure 4-17. The droplet on the crescent array shows much higher velocity up to twice and less oscillations in velocity comparing to the droplet on the flat array. The curved shape of the crescent electrodes keeps almost the same actuated contact line during the droplet movement along the microchannel. Thus, it reduces the fluctuations in the velocity at the end of each electrode. However, there is still reduction in the velocity at the electrode ends due to the deformation of the droplet. In the ideal case, the droplet shape on the crescent electrode remains unchanged during the entire movement. Thus, a portion of the contact line with a constant polar angle is affected by the electric field. Consequently, there will be no reduction in the velocity at the end of each electrode.

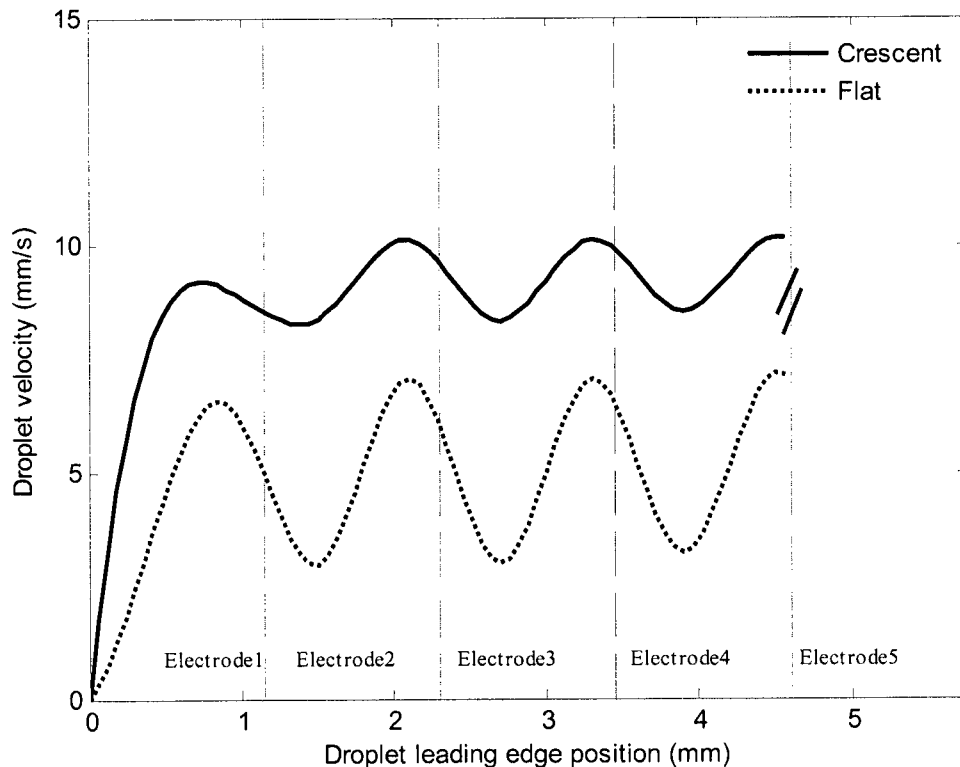


Figure 4-17 Comparison between droplet velocity and oscillation on flat and crescent arrays

5. CLOSURE

This section summarizes all of the chapters of this thesis and remarks the concluding points of this study about the effect of electrode shape in electrowetting-based droplet actuation. Next, it explains the ongoing studies on this subject as well as the potential future work.

5.1. SUMMARY AND CONCLUSIONS

Regarding the performed studies on the electrowetting phenomenon, there has been only a few research conducted on the effect of electrode shape on droplet actuation. Having known the role of the electrode shape in the forces applied on the droplet contact line, this study introduces a novel crescent electrode shape to improve the process of actuation

and movement of the droplet. A combined numerical and experimental work has been performed to prove the superiority of the crescent shape in electrowetting-based droplet manipulation in microchannels. A new implementation of interface voltage has been added to the VOF-based code to better model the droplet actuation specifically at the onset. Several series of experiments illustrated the validation of numerical simulations. The simulations provided detailed information on the voltage distribution on the contact line and showed a larger affected droplet contact line moving on a crescent electrode. This is the reason for having the droplet actuation with less deformation and higher velocities by the crescent electrode. Using this newly designed shape of electrode, the droplet velocities were increased up to twice compared to that of the flat electrode. Moreover, the crescent electrode showed the capability of actuating the droplets even when they are initially away from the electrode by applying a uniform force on the contact line. This shape is proposed to replace the existing traditional electrode shapes due to its excellent performance.

5.2. ONGOING AND FUTURE WORK

The ongoing activities include the experimental validation of numerical results of the droplet movement on the electrode array. These arrays includes flat, crescent with different curvatures and interdigitated electrodes. Additionally, one of the superficial disadvantages which is associated with the crescent shape, would be the movement irreversibility. Using the proposed crescent electrode, we are only able to move the electrode in one way. To resolve this problem, a novel array has been introduced, called “two-way crescent” array. The schematic array and the fabricated one are respectively

shown in Figure 5-1 (a,b). Droplet #1 moves from left to right if electrodes 1 and 2 are fired. The same array moves droplet #2 from right to left if electrodes 7 and 6 are fired. This array not only makes the two-way movement possible, but also it gives the opportunity to have an array with the smaller length electrodes. The latter statement could be explained by the arrangement of charged electrodes. For instance, for moving the droplet from left to right, we can first switch on electrode 1 and after reaching the droplet to the second electrode, we turn it on. As the droplet passes the "football shape" side of the second electrode, electrode 1 can be switched off. This scenario takes place throughout the whole array in both directions to ensure the best performance of this new array. This way, we will have electrodes with smaller length which will result in higher velocities. The switching frequency and the time overlap could be optimized. Several experiments have been already performed on this array which prove its performance.

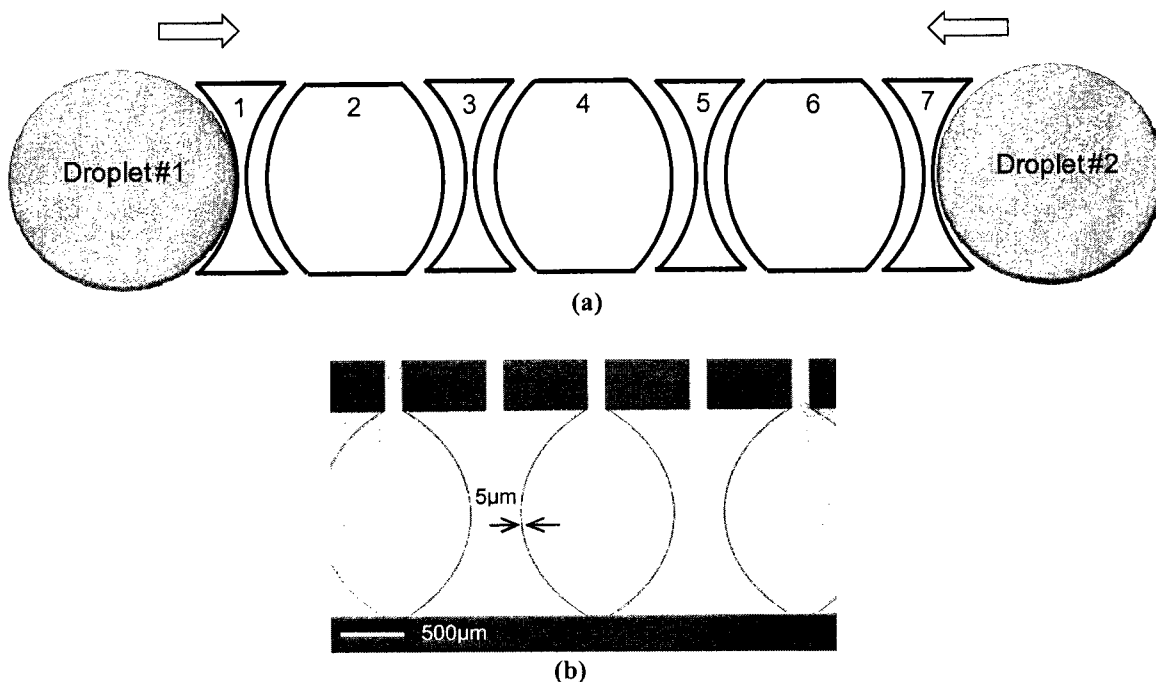


Figure 5-1 Two-way crescent array

The electrodes on an array should be fabricated with a gap in between for individual switching to control the droplet movement. These gaps should be as small as possible to provide the continuous droplet movement. In order to verify the effect of gap size in the electrowetting phenomenon, arrays with different gap sizes of 5, 10 and 20 μm have been fabricated. Another step of this study could be the numerical and experimental research on the existing arrays with different gap sizes.

Ultimately, LOC devices are mainly utilised in biomedical devices where biofluids such as proteins, blood, buffers and DNA are tested. These fluids behave as non-Newtonian fluids which have different governing equations because of their particular characteristics. To compare the experiments of actual samples with the numerical results, the existing code should be customized according to the fluid used in the experiments.

BIBLIOGRAPHY

- [1] Y. Wang, W.Y. Lin, K. Liu, R. J. Lin, M. Selke, H. C. Kolb, N. Zhang, X.Z. Zhao, M. E. Phelps, CK. F. Shen, K. F. Faull, and H. R. Tseng, "An integrated microfluidic device for large-scale in situ click chemistry screening," *Lab on a Chip*, vol. 9, pp. 2281-2285, 2009.
- [2] J. Lienemann, A. Greiner, and J. G. Korvink, "Electrode Shapes for Electrowetting Arrays," *IEEE Transactions on Computer-Aided Design of Integrated Circuits and Systems*, vol. 25, no. 2, 2006.
- [3] M. K. Chaudhury and G. M. Whitesides, "How to make water run uphill," *Science*, vol. 256, pp. 1539-1541, Jun. 1992.
- [4] A. W. Adamson and A. P. Gast, *Physical Chemistry of Surfaces, John Wiley and Sons, Inc., 6th edition*, 1997.
- [5] E. B. Dussan, "On the spreading of liquids on solid surfaces: static and dynamic contact lines," *Ann. Rev. Fluid Mech.*, vol. 11, pp. 371-400, 1979.
- [6] V. Bahadur and S. V. Garimella, "An energy-based model for electrowetting-induced droplet actuation," *J. Micromech. Microeng.*, vol. 16, pp. 1494-1503, 2006.

- [7] G. Beni, S. Hackwood, and J. L. Jackel, "Continuous electrowetting effect," *Appl. Phys. Lett.*, vol. 40, no. 10, pp. 912-914, 1982.
- [8] J. Lee and C. J. Kim, "Liquid micromotor driven by continuous electrowetting," in *IEEE MEMS 98*, Heidelberg, Germany, Jan. 1998, pp. 538-543.
- [9] J. L. Jackel, S. Hackwood, and G. Beni, "Electrowetting optical switch," *Appl. Phys. Lett.*, vol. 40, no. 1, pp. 4-6, 1982.
- [10] M. Washizu, "Electrostatic actuation of liquid droplets for microreactor applications," *IEEE Transaction on Industry Applications*, vol. 34, no. 4, pp. 732-737, 1998.
- [11] M. G. Pollack, "Electrowetting-based microactuation of droplets for digital microfluidics," PhD thesis, Duke University, Durham, NC, USA, 2001.
- [12] M. G. Pollack, A. D. Shenderov, and R. B. Fair, "Electrowetting-based actuation of droplets for integrated microfluidics," *Lab on a Chip*, vol. 2, pp. 96-101, 2002.
- [13] P. Paik, V. K. Pamula, M. G. Pollack, and R. B. Fair, "Electrowetting-Based Droplet Mixers for Microfluidic Systems," *Lab on a Chip*, vol. 3, no. 1, pp. 28-33, 2003.
- [14] P. Paik, V. K. Pamula, and R. B. Fair, "Rapid Droplet Mixers for Digital Microfluidic Systems," *Lab on a Chip*, vol. 3, no. 4, pp. 253-259, 2003.
- [15] V. Srinivasan, V. K. Pamula, and R. B. Fair, "A Droplet-Based Microfluidic Lab-on-a-Chip for Glucose Detection," *Analytica Chimica Acta*, vol. 507, no. 1, pp. 145-

150, 2004.

- [16] V. Srinivasan, V. K. Pamula, M. G. Pollack, and R. B. Fair, "Clinical Diagnostics on Human Whole Blood, Plasma, Serum, Urine, Saliva, Sweat, and Tears on a Digital Microfluidic Platform," in *7th Int'l Conf. Micro Total Analysis Systems (MicroTAS 03)*, 2003, pp. 1287-1290.
- [17] B. Berge and J. Peseux, "Variable focal lens controlled by an external voltage: an application of electrowetting," *Eur. Phys. J.*, vol. 3, p. 159, 2000.
- [18] S. Yang, T. N. Krupenkin, P. Mach and E. A. Chandross, "Tunable and latchable liquid microlens with photopolymerizable components," *Adv. Mater.*, vol. 15, p. 940, 2003.
- [19] S. Kuiper and B. H. W. Hendriks, "Variable-focus liquid lens for miniature cameras," *Appl. Phys. Lett.*, vol. 85, p. 1128, 2004.
- [20] J. Heikenfeld and M. Dhindsa, "Electrowetting on Superhydrophobic Surfaces: Present Status and Prospects," *Journal of Adhesion Science and Technology*, vol. 22, pp. 319-334, 2008.
- [21] M. Gong and C. J. Kim, "Two-dimensional digital microfluidic system by multilayer printed circuit board," in *18th IEEE International Conference on MEMS*, 2005, pp. 726-729.
- [22] J. Gong and C. J. Kim, "Direct-referencing Two-dimensional-array Digital Microfluidics Using Multi-layer Printed Circuit Board," *J Microelectromech Syst.*,

- vol. 17, no. 2, p. 257–264, 2008.
- [23] M. Abdelgawad and A. R. Wheeler, "Low-cost, rapid-prototyping of digital microfluidics devices," *Microfluid Nanofluid*, vol. 4, p. 349–355, 2008.
- [24] U. C. Yi and C. J. Kim, "Characterization of electrowetting actuation on addressable single-side coplanar electrodes," *J. Micromech. Microeng.*, vol. 16, p. 2053–2059, 2006.
- [25] B. Shapiro, H. Moon, R. Garrell, and C. J. Kim, "Equilibrium behaviour of sessile drops under surface tension applied external fields and material variations," *J. Appl. Phys.*, vol. 93, no. 9, 2003.
- [26] J. Monnier, P. Witomski, P.C.W.Bom, and C. Scheid, "Numerical Modeling of Electrowetting by a Shape Inverse Approach," *SIAM J. Appl. Math.*, vol. 69, no. 5, Feb. 2009.
- [27] S. W. Walker, B. Shapiro, "Modeling the fluid dynamics of electrowetting on dielectric (EWOD) ," *Journal of microelectromechanical systems*, vol. 15, no. 4, pp. 986-1000, 2006.
- [28] D. Chatterjee, H. Shepherd, and R. L. Garrell, "Electromechanical model for actuating liquids in a two-plate droplet microfluidic device," *Lab on a Chip*, Feb. 2009.
- [29] A. Nadim, "Electrowetting and Digital Microfluidics," in *The annual meeting of the*

The Mathematical Association of America (MathFest), 2009.

- [30] J. Zeng and T. Korsmeyer, "Principles of droplet electrohydrodynamics for lab-on-a-chip," *Lab on a chip*, vol. 4, pp. 265-277, 2004.
- [31] J. S. Hong , S. H. Ko , K. H. Kang and I. S. Kang, "A numerical investigation on AC electrowetting of a droplet," *Microfluidics and Nanofluidics*, vol. 5, no. 2, pp. 263-271, Aug. 2008.
- [32] A. Dolatabadi, K. Mohseni, and A. Arzpeyma, "Behaviour of a moving droplet under electrowetting actuation: Numerical simulation," *Canadian Journal of Chemical Engineering*, vol. 84, no. 1, pp. 17-21, 2006.
- [33] A. Arzpeyma, "Numerical investigation of droplet actuation via electrowetting in microchannels," MAsc thesis, Concordia University, Montreal, 2007.
- [34] A. Arzpeyma, S. Bhaseen, A. Dolatabadi, P.M. Wood-Adams, "A coupled electrohydrodynamic numerical modeling of droplet actuation by electrowetting," *Colloids and Surfaces A: Physicochemical and Engineering Aspects*, vol. 323, p. 28–35, 2008.
- [35] Z. K. Motamed, L. Kadem, A. Dolatabadi , "Effects of dynamic contact angle on numerical modeling of electrowetting in parallel plate microchannels," *Microfluidics and Nanofluidics*, 2009.
- [36] <http://www.susqu.edu/brakke>.

- [37] M. Bussmann, "A Three-Dimensional Model of an Impacting Droplet," PhD Thesis, University of Toronto, 2000.
- [38] M. Bussmann, J. Mostaghimi, and S. Chandra, "On a three-dimensional volume tracking model of droplet impact," *Phys Fluids.*, vol. 11, no. 6, pp. 1406-1417, 1999.
- [39] D. B. Kothe, R. C. Mjolsness, and M. D. Torrey, "RIPPLE: A computer program for incompressible flows with free surfaces," Technical Report LA-12007-MS. LANL., 1991.
- [40] D. B. Kothe and R. C. Mjolsness, "RIPPLE: A new model for incompressible flows with surface tension," *AIAA J.*, vol. 30, p. 2694, 1992.
- [41] F. H. Harlow and J. E. Welch, "Numerical calculation of time-dependent viscous incompressible flow of fluid with free surface," *Phys. Fluids*, vol. 8, no. 12, pp. 2182-2189, 1965.
- [42] J. E. Welch, F. H. Harlow, J. P. Shannon, and B. J. Daly, "The MAC method," LANL, Technical Report LA-3425, 1966.
- [43] C. W. Hirt, B. D. Nichols, "Volume of fluid /VOF/ method for the dynamics of free boundaries," *Journal of Computational Physics*, vol. 39, pp. 201-225, Jan. 1981.
- [44] W. J. Rider and D. B. Kothe, "Reconstructing volume tracking," *J. Comput. Phys.*, vol. 141, pp. 112-152, 1998.
- [45] L. D. Landau and E. M. Lifshitz, *Fluid Mechanics*, Pergamon Prerss, Oxford 2nd

edition, p. 241, 1987.

- [46] J. U. Brackbill, D. B. Kothe, and C. Zang, "A continuum method for modeling surface tension," *J. Comput. Phys.*, vol. 100, p. 335, 1992.
- [47] T. D. Blake, "The physics of moving wetting lines," *J Colloid and Interface Science*, vol. 299, pp. 1-13, 2006.
- [48] S. V. Mourik, A. E. P. Veldman, and M. E. Dreyer, "Simulation of capillary flow with a dynamic contact angle," *J Microgravity-Science and Technology*, vol. 17, pp. 87-93, 2005.
- [49] T. D. Blake, "Dynamic contact angles and wetting kinetics," *Berg J.C. (Ed.) Wettability. Marcel Dekker, New York*, p. 251–309, 1993.
- [50] S. Glasstone, K. J. Laidler, and H. J. Eyring, *The theory of rate processes*. New York: McGraw-Hill, 1941.
- [51] H. Ren, R. B. Fair, M. G. Pollack, and E. J. Shaughnessy, "Dynamics of electro-wetting droplet transport," *J. Sensors and Actuators B*, vol. 87, pp. 201-206, 2002.
- [52] K. L. Wang and T. B. Jones, "Electrowetting Dynamics of Microfluidic Actuation," *Langmuir*, vol. 21, pp. 4211-4217, 2005.
- [53] J. H. Chen and W. H. Hsieh, "Electrowetting-induced capillary flow in a parallel-plate channel," *J Colloid and Interface Science*, vol. 296, pp. 276-283, 2006.

- [54] C. Decamps and J. Coninck, "Dynamics of spontaneous spreading under electrowetting Conditions," *Langmuir*, vol. 16, pp. 10150-10153, 2000.
- [55] T. D. Blake, A. Clarke, and E. H. Stattersfield, "An investigation of electrostatic assist dynamic contact wetting," *Langmuir*, vol. 16, pp. 2928-2935, 2000.
- [56] "Mask Design Guide for the EVG620 aligner," McGill MicroFab Documents, 2006.
- [57] "Denton RF/DC sputter – user manual," McGill MicroFab Documents, 2006.
- [58] "Denton Vacuum Explorer Coating System Operating Manual," McGill MicroFab Documents.
- [59] "Standard Operating Procedure: Solvent Clean," McGill MicroFab Documents, 2005.
- [60] "MRC 603 Metal Sputter Operation," McGill MicroFab Documents, 2006.
- [61] "Tencor P1 profilometer user manual," McGill MicroFab Documents, 2005.
- [62] "BidTec Spin-Coater User Manual," McGill MicroFab Documents, 2005.
- [63] "Top and Bottom Side lithography – EVG620 user manual," McGill MicroFab Documents, 2005.
- [64] J. B. Fortin and T. M. Lu, *Chemical vapor deposition polymerization: the growth and properties of parylene thin films*. Norwell, Massachusetts, USA: Kluwer Academic Publishers, 2004.

- [65] W. Gorham, "A New, General Synthetic Method for the Preparation of Linear Poly-p-xylylenes," *J. Polym. Sci. Part A-1*, vol. 4, p. 3027, 1966.
- [66] "Vacuum Plymer Deposition System Manual - Model: PARA-10S," *Advancing Plasma-Based Thechnologies - Plasmionique*.
- [67] J. F. O'Hanlon, "A User's Guide to Vacuum Technology, 2nd Ed," in *A User's Guide to Vacuum Technology*. New York: Wiley, 1989, ch. 3.
- [68] C. E. Morossanu, "Thin films by Chemical Vapor Deposition," in *Thin films by Chemical Vapor Deposition*. New York: Elsevier, 1990, ch. 5.

APPENDIX A: PARYLENE

DEPOSITION FORMULAS ^[64]

Calculation of pumping speed and flow rate

Following method can be used to obtain the approximate pump speed,

- 1) System is pumped to its base pressure, P₁, the vacuum valve is closed, and the pressure rise is measured, dP₁/dt.
- 2) Vacuum valve is opened, system is pumped back to its base pressure, and gas is admitted until a stable pressure, P₂, is reached.
- 3) Vacuum valve is closed again and dP₂/dt is measured.
- 4) System volume is measured.

Pumping speed is calculated using following equation:

$$S = V \left(\frac{\left(\frac{dP_2}{dt} - \frac{dP_1}{dt} \right)}{P_2 - P_1} \right)$$

S is pump speed in L/sec, V is the volume in L, P is pressure in mtorr, and t is time in seconds [67].

The flow rate, Q can be calculated: Q=SP

Q is in units of L-Torr/sec and can be converted to sccm.

The pressure rises were measured and automatically recorded via computer for a number of pressures in the typical deposition range. The nearly instantaneous pressure changes as a function of time were found from the slope of the pressure versus time data over a period of a few seconds. The volume of the system was measured by attaching a small reservoir of known volume to the evacuated chamber with a valve in between. This valve was opened to allow a known volume of air to enter the chamber and the pressure rise was recorded. The volume was then calculated using gas laws.

Calculating the residence time

The residence time of a gas in a deposition chamber or in a tube through which the gas flows into the chamber can be calculated using the expression $t = L/V_m$. t is the contact time in seconds, L is the length of the tube in cm, and V_m is the rate of gas flow in mL/cm^2sec and can be found from $V_m = D/S$ where D is the total gas flow rate in ml/sec and S is the cross sectional area of the tube in cm^2 [68].

The information got for any deposition system, can be helpful to researchers or process development engineers to determine the appropriate temperature range for 100% conversion without an excessive thermal budget.

Kinetic Modeling of Parylene Thin Film Growth (deposition rate calculation)

Several models have been developed to predict the deposition rate as a function of monomer pressure and substrate temperature. The models are categorized into four different types: Flory-type adsorption, Langmuir-type adsorption, Brunauer-Emmett-Teller (BET-type) adsorption and chemisorption models. First three models are derived

based on the monomer concentration at the surface of the growing film. Beach's equation for the deposition rate read as:

$$R_d = \left(\frac{2k_i k_p D_f^2}{3\rho^3} \right)^{1/4} (C_{M,S}^F)^{3/2}$$

Where k_i , k_p and D_f are the initiation rate constant, the propagation rate constant, and the diffusion constant of monomer through the polymer film, respectively. The concentration at the surface of the growing film is given by Flory,

$$C_{M,S}^F = \frac{\rho P}{K_H P_{sat}}$$

Where $C_{M,S}^F$ is the surface concentration of the adsorbed monomer, ρ is the density of the film, P is the pressure in the deposition chamber, K_H is the dimensionless constant with a value near 3, and P_{sat} is the equilibrium vapour pressure of the monomer at the given temperature.

All these three models contain terms for the kinetics of the initiation reaction, propagation reaction, and sometimes, the diffusion of monomer into the bulk which makes them complicated. The Chemisorption model is based on the maximum deposition rate for any CVD process which is given by,

$$R_d = \frac{SPN_a V_m (60 \times 10^{10})}{(2\pi m_r RT_o)^{0.5}}$$

Where the quantity $PN_a/(2\pi m_r R_o)^{0.5}$ is the flux of the reactant to the substrate surface, P is the pressure, N_a is Avogadro's number, m_r is the molecular mass, R is the Rydeberg

gas constant, and T_o is the temperature of the gas, V_m is the volume of one molecule and S is the sticking coefficient.

In the case of Langmuir type adsorption the sticking coefficient is given as $S = S_o(1 - \theta)$ in which $(1 - \theta)$ is the fraction of the surface sites that are reactive or are radical chain ends.

Chemisorption model fits the data better than any of the other models and the values of the fit parameters are sufficiently reasonable. A detailed analysis of how a parameter should affect the deposition rate for each of the control types is given in [68].

The effect of changing substrate temperature and pressure on the deposition rate as well as on film properties has been studied by many researchers. All reports show an increase in deposition rate with a decrease in temperature. They also showed deposition rates that were proportional to p^1 , $p^{3/2}$, p^2 . Therefore, the deposition rate increases as the substrate temperature is decreased and as the monomer pressure is increased. There is also a minimum pressure below which no deposition occurs. This pressure increases as substrate temperature increases.